

The Properties of Cosmic Velocity Fields

Oliver Hahn^{1*}, Raul E. Angulo² & Tom Abel³

¹*Department of Physics, ETH Zurich, CH-8093 Zürich, Switzerland*

²*Centro de Estudios de Física del Cosmos de Aragón, San Juan, 1 Planta-2, 44001 Teruel, Spain*

³*Kavli Institute for Particle Astrophysics and Cosmology, Stanford University, SLAC National Accelerator Laboratory, Menlo Park, CA 94025, USA*

submitted to MNRAS

ABSTRACT

Understanding the velocity field is very important for modern cosmology: it gives insights to structure formation in general, and also its properties are crucial ingredients in modelling redshift-space distortions and in interpreting measurements of the kinetic Sunyaev-Zeldovich effect. Unfortunately, characterising the velocity field in cosmological N -body simulations is inherently complicated by two facts: i) The velocity field becomes manifestly multi-valued after shell-crossing and has discontinuities at caustics. This is due to the collisionless nature of dark matter. ii) N -body simulations sample the velocity field only at a set of discrete locations, with poor resolution in low-density regions. In this paper, we discuss how the associated problems can be circumvented by using a phase-space interpolation technique. This method provides extremely accurate estimates of the cosmic velocity fields and its derivatives, which can be properly defined without the need of the arbitrary “coarse-graining” procedure commonly used. We explore in detail the configuration-space properties of the cosmic velocity field on very large scales and in the highly nonlinear regime. In particular, we characterise the divergence and curl of the velocity field, present their one-point statistics, analyse the Fourier-space properties and provide fitting formulae for the velocity divergence bias relative to the non-linear matter power spectrum. We furthermore contrast some of the interesting differences in the velocity fields of warm and cold dark matter models. We anticipate that the high-precision measurements carried out here will help to understand in detail the dynamics of dark matter and the structures it forms.

Key words: cosmology: theory, dark matter, large-scale structure of Universe – galaxies: formation – methods: N -body, numerical

1 INTRODUCTION

N -body simulations in computational cosmology (e.g. Melott 1982; Efstathiou et al. 1985; Peebles et al. 1989; Springel 2005; Angulo et al. 2012) are an invaluable tool to study the dynamics of cosmic dark matter over time. Statistics of the dark matter velocity field are important for cosmological measurements of redshift-space distortions from galaxy surveys (see e.g. Dekel 1994, for a classic review), of the kinetic Sunyaev-Zeldovich effect, as well as for more theoretically motivated questions regarding the formation and dynamics of the cosmic large-scale structure (e.g. Bertschinger & Dekel 1989; Bernardeau & van de Weygaert 1996; Pichon & Bernardeau 1999; Pueblas & Scoccimarro 2009; Kitaura et al. 2012).

Unfortunately, there is a fundamental problem when determining the dark matter velocity field from N -body simulations: while the velocity field is defined everywhere in space in the continuous limit, in simulations it is sampled only at the (mass-

weighted) particle positions. A recent discussion by Jennings et al. (2011) highlights the potentially large uncertainties on different measures of the velocity power spectrum from cosmological N -body simulations. Using a standard cloud-in-cell (CIC Hockney & Eastwood 1981) deposit to project simulation results on a grid leads to unacceptable levels of noise and biases, severely complicating a reliable measurement of this quantity.

Various approaches can be found in the literature to reconstruct a continuous velocity field and address this sampling issue. One possibility is to apply a large-scale smoothing (i.e. using a kernel estimator) with a given fixed or adaptive kernel function (e.g. Bertschinger & Dekel 1989; Melott & Shandarin 1993). This has advantages when applied to galaxy catalogs and the interest is mostly limited to the large scales that are still close to the linear regime and where shell-crossing can be neglected. Another approach is based on using inverse SPH-smoothed velocity fields (Colombi et al. 2007). A third class of approaches employs tessellations of the spatial distribution of sampling points which yields a good estimator in the absence of shell-crossing. Tessellations allow to define unique volumes

* Email: hahn@phys.ethz.ch

around particles (by Voronoi tessellations) or by connecting the particles (Delaunay triangulations: e.g. Icke & van de Weygaert 1987; Bernardeau & van de Weygaert 1996; Pueblas & Scoccimarro 2009), and they have been particularly popular in recent analyses of N -body simulations (e.g. Pandey et al. 2013). As shown by Bernardeau & van de Weygaert (1996) and Pueblas & Scoccimarro (2009), Delaunay tessellations of the particle distribution can be used to better control noise and measurement errors of velocity power spectra from N -body simulations. In addition, Jennings (2012) showed that the DTFE estimator (Schaap & van de Weygaert 2000; Pelupessy et al. 2003; Schaap 2007), as implemented by Cautun & van de Weygaert (2011), gives much more reliable spectral properties compared to fixed kernel smoothing (confirming a similar finding by Pueblas & Scoccimarro 2009).

Despite recent progress, while trying to solve the two issues described above, these methods sacrificed a direct measurement of the velocity field by that of a smoothed field and/or introduced high levels of noise. This is particularly important: due to the collisionless nature of dark matter, gravitational collapse leads to a multi-valued velocity field in multi-stream regions (quite in contrast to the behaviour of an ideal fluid), and discontinuities appear in the velocity field. Therefore, as we will discuss throughout this paper, the properties of the volume-averaged (i.e. "coarse-grained") velocity field are not identical to the properties of the mean velocity field. For instance, a non-zero vorticity appears in the coarse-grained velocity field even in regions with particles whose orbits have not yet crossed. Additionally, the properties of the coarse-grained field strongly depend on the (arbitrary) scale on which the volume average is performed.

In this paper, we will demonstrate how the mean velocity field and its differential properties (specifically, its vorticity and divergence) can be computed avoiding the problems outlined above. In particular, we will propose a scheme that provides an accurate (and to our knowledge the only) way to determine the mean velocity field without coarse-graining and in the presence of multi-streaming. This is a direct consequence of the possibility to define an explicit projection from phase-space into configuration space based on a reconstruction of the fine-grained distribution function. Therefore, and in contrast to coarse graining, there is no arbitrary scale in this direct projection.

Our approach is based on the method to analyse cosmological N -body simulations proposed by Abel et al. (2012) (AHK12 hereafter). The key idea rests on the fact that structure formation in cold dark matter starts out on a very thin sheet in configuration space with an almost infinitesimally small extent in velocity space. Consequently, one can think of the modelled particles as the moving (massless) vertices of a tessellation of this initial (Lagrangian) phase space sheet. Shandarin et al. (2012) independently developed the same idea with only minor differences in the implementation. The estimates of densities, velocities and velocity dispersion therefore incorporate the information of neighbouring particles in phase-space. Such a Lagrangian tessellation is able to accurately represent anisotropic deformations of the density field which allows it to be free from the artificial clumping seen in (adaptive) kernel smoothing (Hahn et al. 2013; Angulo et al. 2013).

The features described above make this method unique from all other methods such as adaptive kernel smoothing (as e.g. in SPH Monaghan 1992), CiC deposits or DTFE. We also note that our method is distinct from the phase space estima-

tion techniques of Sharma & Steinmetz (2006) or Ascasibar (2010), which treat N -body data results as Monte Carlo sampled realisations of the micro-physical phase space structure of the dark matter distribution. Consequently all these methods are subject to noise even in the case of the heavily smoothed SPH method (see the detailed discussion in Hahn et al. 2013).

Using our explicit phase-space projection procedure applied to dark matter N -body simulations, we are able to (i) show how the velocity field switches from convergent to divergent flow in multi-stream regions, with a remnant convergent core in the centres of high-density structures such as haloes and filaments; (ii) demonstrate that vorticity is a multi-stream phenomenon, which peaks at caustics; (iii) present the 1-point statistics of the velocity divergence and vorticity, and (iv) provide high-resolution Fourier-space properties of the velocity field, in terms of velocity divergence and vorticity power spectra, and density-divergence cross-spectra. We also provide fitting formulae for the velocity divergence bias relative to the non-linear matter power spectrum. We furthermore contrast some of the interesting differences in the velocity fields of warm and cold dark matter models. All our results are presented in Sections 4 and 5.

The structure of this paper is as follows: We first discuss how mean velocity fields are defined through a projection operation and give special attention to derivatives of the projected velocity field that are non-trivial to compute due to the discontinuous nature of the field in Section 2. Next, in Section 3, we introduce the N -body simulations used in this work. In Section 4, we present an analysis of the real-space properties of the velocity field. In Section 5, we focus on the spectral properties of velocity fields computed with our method and provide fits for the Fourier space k -dependent bias of the velocity divergence relative to the cosmic density field. We summarise our results in Section 6.

2 PROJECTIONS ONTO CONFIGURATION SPACE, DERIVATIVE OPERATORS AND DIFFERENTIALS OF VECTOR FIELDS

In this section, we discuss how to obtain mean velocity fields from N -body simulations using the cold dark matter sheet by projecting the fine-grained distribution function from phase space onto configuration space. We then discuss the differential properties of such projected fields. We will argue that these differentials cannot in general be approximated by finite differences and derive the correct expressions for the divergence and the curl of the projected velocity field. Finally, we discuss how a piecewise linear approximation to the fine-grained distribution function based on N -body particles, as introduced in AHK12, can be used to compute the velocity field and its differentials from simulations.

2.1 The Vlasov-Poisson system and the distribution function of cold fluids

We are concerned here with the mean velocity field of cold dark matter, a cold collisionless self-gravitating fluid. The evolution of such a fluid is fully described by the phase-space distribution function $f(\mathbf{x}, \mathbf{v}, t)$ governed by the Vlasov-Poisson system of equations (see e.g. Peebles 1980; Henon 1982, the latter for a historical discussion)

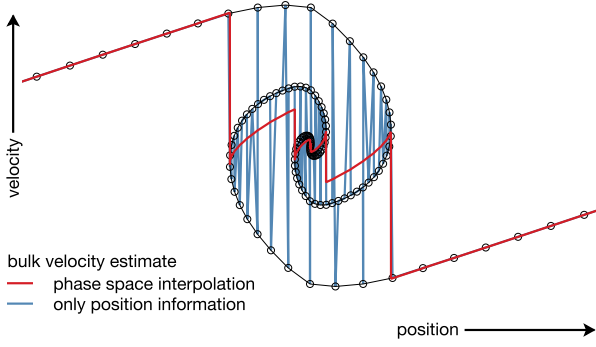


Figure 1. Using tessellations to measure cosmic velocity fields: Estimation of the mean velocity in a one-dimensional plane wave collapse problem when only position information is available for the tessellation (blue), or when the full phase space information can be used (red). Black circles show the positions of the particles used in the simulation, black lines indicate their connectivity on the dark matter sheet and thus provide a piecewise linear approximation to the fine-grained distribution function.

$$0 = \frac{df(\mathbf{x}, \mathbf{v}, t)}{dt} = \frac{\partial f}{\partial t} + \frac{\mathbf{v}}{a^2} \cdot \nabla_{\mathbf{x}} f - \nabla_{\mathbf{x}} \phi \cdot \nabla_{\mathbf{v}} f, \quad (1)$$

$$\nabla_{\mathbf{x}}^2 \phi = \frac{4\pi G}{a^3} \int d^3v (f - \bar{\rho}), \quad (2)$$

where G is the gravitational constant, a is the cosmological scale factor that itself obeys the first Friedmann equation, and $\bar{\rho}$ is the mean density. The full phase space distribution function $f(\mathbf{x}, \mathbf{v}, t)$ is in general manifestly six-dimensional. For a perfectly cold fluid however, the distribution function occupies only a three-dimensional hypersurface (in fact a sub-manifold) of six-dimensional phase space (see e.g. the discussion in Abel et al. 2012; Shandarin et al. 2012). We can thus express the distribution function through a parametrization of the hypersurface $\mathbb{R}^3 \rightarrow \mathbb{R}^6 : \mathbf{q} \mapsto (\mathbf{x}_{\mathbf{q}}, \mathbf{v}_{\mathbf{q}})$ in terms of ‘‘Lagrangian coordinates’’ \mathbf{q} . The particles of an N -body simulation can be thought of as a finite sampling $\mathbf{q}_i \in \mathbb{R}^3$, $i = 1 \dots N$ of this hypersurface.

We note that the density is given by a projection of the distribution function itself onto configuration space $\rho(\mathbf{x}, t) \equiv \int d^3v f(\mathbf{x}, \mathbf{v}, t)$. In the case of a cold fluid, the integral over velocity space becomes a discrete sum over the streams overlapping a given point. For the notation, we omit the explicit time dependence in what follows.

2.2 The mean velocity field

The mean velocity is obtained from the first velocity moment of the distribution function, i.e. the following projection onto configuration space

$$\langle \mathbf{v} \rangle \equiv \frac{\int_{\mathbb{R}^3} \mathbf{v} f(\mathbf{x}, \mathbf{v}) d^3v}{\int_{\mathbb{R}^3} f(\mathbf{x}, \mathbf{v}) d^3v} = \frac{\sum_{s \in S(\mathbf{x})} \mathbf{v}_s(\mathbf{x}) \rho_s(\mathbf{x})}{\sum_{s \in S(\mathbf{x})} \rho_s(\mathbf{x})}, \quad (3)$$

where $S(\mathbf{x})$ is the set of all streams s that contain point \mathbf{x} , a subscript s indicates the value of a field at \mathbf{x} on a given sheet, and the second equality holds for cold fluids, as discussed above. The mean velocity field is thus given by a density-weighted average over the multi-stream velocity field (cf. Fig. 1). We want to remark explicitly that our projection operator $\langle \cdot \rangle$ does

not involve the convolution with a smoothing kernel as is often done. We note also that this projection operator, unlike kernel smoothing, is explicitly idempotent, i.e. $\langle \langle \cdot \rangle \rangle = \langle \cdot \rangle$.

2.3 Differentials of velocity fields

The differential flow properties of fluids are typically discussed in terms of the various components that contribute to the first derivative – i.e. the velocity gradient tensor $\nabla \otimes \mathbf{v}$ – of the the flow velocity field. This velocity gradient tensor is then further decomposed into (1) its trace, the velocity divergence $\text{div } \mathbf{v} = \nabla \cdot \mathbf{v}$, (2) the anti-symmetric part of the tensor yields the vorticity vector $\boldsymbol{\omega} = \text{curl } \mathbf{v} = \nabla \times \mathbf{v}$, and (3) the symmetric trace-free part of the tensor is the velocity shear $S_{ij} = \frac{1}{2} (\nabla \otimes \mathbf{v} + (\nabla \otimes \mathbf{v})^T)$, which we will however not consider further in this paper. The scalar magnitude of the vorticity vector field we call simply ‘‘vorticity’’ $\omega = \|\boldsymbol{\omega}\|$.

We note that vorticity does not appear before shell-crossing if the velocity field is not sourced by a vector potential and vorticity is initially zero (this can also be seen simply as a consequence of Helmholtz’s circulation theorem). If initial vorticity is present, it is conserved and will be amplified by gravitational collapse (cf. Buchert 1992), but typically vortical initial modes are ignored, as we will also do in this paper. Then, in the case of Newtonian gravity, the acceleration is given by the gradient of the gravitational potential ϕ . Hence, the single stream motion of a Lagrangian fluid element $(\mathbf{x}_{\mathbf{q}}, \mathbf{v}_{\mathbf{q}})$ is curl-free non-perturbatively at all times since at fixed \mathbf{q} : $\frac{d}{dt} \nabla \times \mathbf{v}_{\mathbf{q}} = -\nabla \times \nabla \phi|_{\mathbf{x}_{\mathbf{q}}} = 0$ if it is irrotational initially (cf. also Bernardeau et al. 2002). After shell-crossing, various fluid elements overlap and vorticity emerges (cf. also Pichon & Bernardeau 1999), as we will discuss further below.

2.4 Differentials of the projected multi-stream velocity field

As we will see next, the differentials of a projected variable are singular at the location of caustics where the number of streams changes and the projected field has a discontinuity. This can be easily seen directly from the definition of a derivative applied to a projected field $\langle g \rangle$:

$$\frac{d \langle g(x) \rangle}{dx} = \lim_{h \rightarrow 0} \frac{\langle g(x+h) \rangle - \langle g(x) \rangle}{h}. \quad (4)$$

The right-hand-side can be written as

$$\lim_{h \rightarrow 0} \frac{1}{h} \frac{\sum_{s \in S_1} \sum_{t \in S_2} \rho_s(x+h) \rho_t(x) (g_s(x+h) - g_t(x))}{\sum_{s \in S_1} \sum_{t \in S_2} \rho_s(x+h) \rho_t(x)}, \quad (5)$$

where we note that S_1 (containing points $x+h$) and S_2 (containing points x) can in general be sums over different numbers of streams so that the change in the number of streams has to be taken into account when performing the limit (cf. Fig. 2 and our discussion below); g_s and g_t indicate the values of g on the various intersection points of the sheet with points $x+h$ and x respectively.

In what follows, we first discuss the properties of derivatives across such discontinuities before we turn to the properties of derivatives away from discontinuities which is almost everywhere (in the mathematical sense) in configuration space.

We wish to remark that this division of space into regions where the derivative is non-singular (i.e. away from caustics) and regions of singular derivatives of measure zero is only possible with the proposed explicit phase-space projection

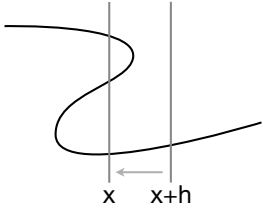


Figure 2. Illustration of a small piece of a cold distribution function in 1+1 dimensional phase space (black line). The vertical direction represents velocity, while the horizontal direction represents the spatial dimension. When computing spatial derivatives of projected fields, the difference evaluated on a finite interval does not approach the derivative if the interval contains a caustic which implies a change in the number of streams and a discontinuity in the respective mean velocity field.

method. Any method that uses (implicit) coarse-graining will necessarily include the singularities integrated over the coarse-graining scale in configuration space (see below) although (without coarse-graining) these regions should not contribute to any volume averages due to their zero volume measure when no coarse-graining is performed.

Derivatives across discontinuities: As we are concerned here with projections into configuration space of the fine-grained distribution function, discontinuities in the projected fields are real discontinuities of infinitesimal extent. Consequentially, the derivative across a discontinuity is a Dirac- δ function, i.e. for a velocity field with left-sided limit v_l and right-sided limit v_r at location x_0 – given generically by $v(x) = (v_r - v_l) \Theta(x - x_0) + v_l$, where Θ is the Heaviside Θ -function – the derivative near x_0 is given by

$$\frac{dv}{dx} = (v_r - v_l) \delta_D(x - x_0). \quad (6)$$

For the three dimensional cold distribution functions we are concerned with here, these singular derivatives of finite measure occupy (one- and) two-dimensional subspaces at the caustic locations. If no coarse-graining is performed, they thus constitute a subset of configuration space that has volume measure zero and is singular. If coarse-graining is performed (i.e. the singular surfaces are convolved with a kernel or simply integrated over a finite volume element), the finite jump $(v_r - v_l)$ is recovered on the scale on which coarse-graining is performed. Any approach to determine velocity fields that involves coarse-graining will thus include contributions from the velocity jump at these discontinuities although the associated volume is zero. The value of these contributions depends explicitly on the coarse-graining scale. The physical meaning of the singular derivatives is that they describe the motion of the caustics themselves. We discuss below how the differential properties of velocity fields can be obtained in a way that excludes the contribution of these singular subspaces – a result that can only be obtained with the explicit projection method of the reconstructed fine-grained distribution function that we discuss here.

Derivatives of projected fields away from discontinuities: Away from discontinuities, derivatives of projected properties ought to be performed using the fine-grained distribution and the explicit derivatives of the projection operator. In general, this will involve non-trivial commutators. It is thus not possible to perform a projection operation onto a mesh and then evaluate derivatives using difference operators on that

mesh without implicitly performing a coarse-graining operation. Below, we explicitly calculate some basic differential operators applied to the projected velocity field. We provide the detailed derivation of the expressions below in appendix A.

Divergence of the velocity field: The velocity divergence naturally already appears at the single-stream level. The divergence of the mean velocity field is given by

$$\nabla \cdot \langle \mathbf{v} \rangle = \langle (\nabla \log \rho) \cdot (\mathbf{v} - \langle \mathbf{v} \rangle) \rangle + \langle \nabla \cdot \mathbf{v} \rangle \quad (7)$$

arising from the sum of a term that is purely due to the projection of a multi-stream field (first term), and which reflects alignment of velocities with density gradients, and the projected single-stream velocity divergence (second term).

Curl of the velocity field: As already discussed above, vorticity vanishes on the fine-grained distribution function and is thus a property of the projected velocity field alone (see also the discussion in, e.g., Pichon & Bernardeau 1999; Wang et al. 2014, on the emergence of vortical flow) and thus a purely collective phenomenon of multi-streaming. It is in full generality given by

$$\nabla \times \langle \mathbf{v} \rangle = \langle (\nabla \log \rho) \times (\mathbf{v} - \langle \mathbf{v} \rangle) \rangle + \langle \nabla \times \mathbf{v} \rangle, \quad (8)$$

but the second term vanishes for gravitationally generated velocities. The form of this equation is reminiscent of the baroclinic term in the vorticity equation of an ideal fluid where vorticity arises from the mis-alignment of density and pressure gradients.

2.5 The case of 1+1 dimensional phase-space

In the case of one spatial and one velocity dimension, the fine-grained distribution function can be approximated by connecting particles that are neighbours in the initial conditions through straight lines. The mass m of one particle can then be thought of as being distributed uniformly along the line element so that the single-stream density at every particle location is simply $\rho = 2m/l$, where $l = \Delta x_{i,i-1} + \Delta x_{i,i+1}$ is the sum of the distances to the neighbouring particles in Lagrangian space. Single-stream velocities and densities can then be linearly interpolated in-between particles. The density and velocity projected into configuration space at an arbitrary location x are readily calculated from the single-stream values by determining which line-elements intersect x and then calculate the weighted averages as discussed above.

In Fig. 1, we show the mean velocity obtained in this way for the late stages of plane-wave collapse (red line). We compare it to the estimate that a Delaunay tessellation approach would give (blue). In this approach, the phase-space connectivity is not respected and only configuration space information is used. Particles that are closest in configuration space are connected by linear elements and velocities are linearly interpolated along these elements. In multi-stream regions this leads to a noisy and incorrect projected velocity field if no coarse-graining is performed.

We can see from Fig. 1 that the mean velocity field (red line) has discontinuities at the caustics and, at that particular time, also has a positive slope everywhere except in the very centre. We argued in the previous subsection that these discontinuities (due to a change in the number of streams) lead to errors when finite differences are used and the finite difference interval brackets a caustic. In Fig. 3, we show the phase-space (top panels) together with the velocity divergence (bottom panels) for the collapse of a plane wave before (left panels)

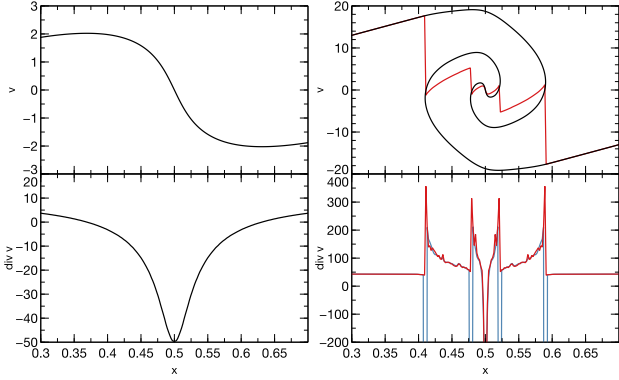


Figure 3. Before shell-crossing (left column), the mean velocity field is identical to the fine-grained (top left) and the velocity divergence (bottom left) is anti-correlated with the overdensity. After shell-crossing (right column), the mean velocity field (red, top right) is different from the fine-grained multi-stream velocity field (black). The velocity divergence (bottom right) estimated directly on the sheet (following eq. 7) is everywhere positive except in the very centre. In contrast, a finite difference estimate computed from gridded values of the mean field (blue) shows a dominant negative velocity divergence at caustics but is slightly less noisy. The negative divergence reflects the finite velocity jump (that is in fact occurring over an infinitesimal volume and is thus not present in the direct projection). The correlation between the velocity divergence and the overdensity field changes its sign except in the innermost region and in the single-stream region.

and after (right panels) shell crossing. Before shell-crossing, the velocity field is single-valued and has negative velocity divergence in the central region $0.4 \lesssim x \lesssim 0.6$. After shell-crossing, the mean velocity field is given by the red line (top right panel) with the properties we have just discussed. If the velocity divergence is computed by applying finite differences to the projected field on a grid (blue line, bottom right panel), the singular derivative (see discussion above) at the caustic locations is effectively integrated over a finite volume so that the finite velocity jump divided by the scale is recovered. If eq. (7) is used to compute the velocity divergence (red line, bottom right panel), i.e. by computing single stream finite differences on the phase space line elements followed by projection onto configuration space, the singular derivative, which exists only at a finite number of points need not be included. As a result, we see that the velocity field is expansive almost everywhere with discontinuous jumps at the caustics.

We observe that the divergence calculated directly from the sheet in the described way is somewhat noisy. This is a consequence of the low-order interpolations we are using. Higher order schemes are expected to improve this but are beyond the scope of this article.

Another interesting observation from Fig. 3 is that, before shell crossing, the velocity divergence is anti-correlated with overdensity – divergence being negative where overdensity is positive – while after shell-crossing this correlation reverses except in the very centre of the collapsed structure where the divergence oscillates between positive and negative. In the 1+1 dimensional case, the velocity divergence of collapsed structures is thus predominantly positive. We will revisit this aspect in the 3+3 dimensional case in Section 4.2.

2.6 Projections of phase space in N -body simulations and the dark matter sheet

In our discussion above, we have argued that knowledge of the distribution function is *necessary* to accurately perform its projection onto configuration space and thus determine the mean velocity field *without performing a coarse-graining operation*. As we have discussed in AHK12, the fine-grained distribution function of cold dark matter can be reconstructed from N -body simulations using the phase-space sheet tessellation method described there. In this method, a tessellation of the Lagrangian particle coordinates \mathbf{q} is performed, decomposing the entire particle distribution into a collection of tetrahedral phase space elements.

Since, due to Liouville’s theorem, the tessellation is preserved in phase space, it can be reconstructed at any later time if the connectivity is known. In the case of an initial cubical lattice of particles, this is particularly simple since the three-dimensional Lagrangian coordinate can be encoded in the particle IDs, and the connectivity can be determined on-the-fly. In fact, the entire procedure to know which four particles span every relevant simplex (tetrahedron) of the tessellation reduces to decomposing one unit cube into six tetrahedra of equal size (the Delaunay triangulation of the unit cube). Consequently, one can then think of the data output from a simulation as the information that describes the evolution of the vertices of the $N_{tet} \equiv 6N_p$ tetrahedra. Each of them carries $m_{tet} = M_{box}/N_{tet}$ of the mass M_{box} in the simulation box and represents a piecewise linear interpolation between four vertices on the fine-grained distribution function. In fact, to reduce the possible impact of anisotropies due to the choice of one of the six equivalent Delaunay triangulations of the unit cube, we average over all those six possibilities. Similar methods employing the advection of a tessellation of test particles can be used in simulations of incompressible flows, allowing the calculation of Lagrangian flow properties (e.g. Pumir et al. 2013).

2.6.1 Interpolating and differentiating on tetrahedra

For a tetrahedron with vertices $\mathbf{x}_k = (x_k, y_k, z_k)$, $k = 1 \dots 4$, any point $\mathbf{x} = (x, y, z) = (x_i)$, $i = 1 \dots 3$, can be expressed in terms of *tetrahedral coordinates* $\boldsymbol{\zeta} = (\zeta_1, \zeta_2, \zeta_3, \zeta_4)$ through the linear transformation

$$(1, x, y, z)^T = \begin{bmatrix} 1 & 1 & 1 & 1 \\ x_1 & x_2 & x_3 & x_4 \\ y_1 & y_2 & y_3 & y_4 \\ z_1 & z_2 & z_3 & z_4 \end{bmatrix} \cdot \boldsymbol{\zeta}^T =: \mathbf{J} \cdot \boldsymbol{\zeta}^T. \quad (9)$$

It is easy to see that $\sum_k \zeta_k = 1$ and the volume of the tetrahedron is simply $V = \frac{1}{6} |\det \mathbf{J}|$. For any field F whose values are known at the vertices \mathbf{x}_k , i.e. $F_k = F(\mathbf{x}_k)$, the linear interpolation to an arbitrary point \mathbf{x} can then be written as

$$F[\boldsymbol{\zeta}(\mathbf{x})] = \sum_{k=1 \dots 4} F_k \zeta_k(\mathbf{x}). \quad (10)$$

This implies that differentials of F can be obtained through the chain-rule by simply computing

$$\frac{\partial F}{\partial x_i} = \sum_{k=1 \dots 4} \frac{\partial F}{\partial \zeta_k} \frac{\partial \zeta_k}{\partial x_i} = \sum_{k=1 \dots 4} \mathbf{J}_{i+1,k}^{-1} F_k, \quad (11)$$

where the index i refers to a Cartesian coordinate, and *not* to vertex i . Note that a derivative computed in this way is only

accurate at first order (like the simple backward/forward finite difference operators). Gradient operators that are accurate at higher order are of course possible and would include information from more than one tetrahedron or involve quadratic tetrahedra (defined using 10 instead of 4 vertices for the linear tetrahedron). We leave this aspect for future work as first order gradients are accurate enough for the purposes of this article. We note however that, for example, a curl-free non-linear field will appear to have curl if evaluated with low-order finite differences. We note that differentials only exist if J is invertible, i.e. if $\det J \neq 0$, which is equivalent to $V \neq 0$.

2.6.2 Determining the fine-grained density and velocity as well as their derivatives

The sheet is parametrised by the Lagrangian coordinate \mathbf{q} and discretised into tetrahedral elements with vertices \mathbf{q}_i . If a piecewise constant density field is sufficient, one can simply use the location of the vertices (particles) to determine the mass density that every tetrahedron contributes to a point inside its volume as $\rho_{\text{tet}} = m_{\text{tet}}/V_{\text{tet}}$, with the tetrahedron volume V_{tet} defined above. As we have discussed in Section 2.4 above, the derivatives of the projected velocity field contain also derivatives of the fine-grained density. Hence, a piecewise constant fine-grained density will not be sufficient. We therefore compute a density estimate at each vertex from the mean volume of all N_{tets} tetrahedra that share a given vertex \mathbf{q}_i . Specifically, the density at a given vertex \mathbf{q}_i is given by $\rho(\mathbf{q}_i) = m_{\text{tet}} N_{\text{tets}} \left[\sum_{j=1 \dots N_{\text{tets}}(\mathbf{q}_i)} V_j \right]^{-1}$, i.e. the reciprocal of the sum over the volumes V_j of all tetrahedra that share the vertex. We note that it is not possible to use the dual Voronoi mesh to obtain a vertex-centered density since the Voronoi cells are not necessarily convex.

Having a density estimate defined at each vertex, we can now linearly interpolate easily to any position \mathbf{x} inside a given tetrahedron using eq. (10). This achieves a piecewise linear field with a piecewise constant derivative across the tessellation. Similarly, for each tetrahedron, the fine-grained velocity $\mathbf{v}_{1 \dots 4}$ is known at the four vertices \mathbf{q}_i and can be linearly interpolated to position \mathbf{x} using eq. (10), and eq. (11) can be used to compute derivatives on each tetrahedron. In this way, the gradient of the fine-grained (i.e. per stream) density field $\nabla \rho$ as well as the gradient tensor of the fine-grained velocity field $\nabla \otimes \mathbf{v}$ can be easily calculated from the values of the density as well as the velocity at the four vertices of each tetrahedron.

2.6.3 Projected fields using the dark matter sheet

To determine the projection of a field $g(\mathbf{q})$, defined on the dark matter sheet, at an arbitrary point \mathbf{x} , we first determine all the tetrahedra which contain \mathbf{x} . The velocity and density due to each stream is computed by linearly interpolating from the four vertices of each tetrahedron to the point. Having now a linearly interpolated quantity $g_i(\mathbf{x})$ for tetrahedron i , we next average over all the tetrahedra i that contain that point and weight each contribution by the density of the tetrahedron, i.e. make the approximation

$$\langle g \rangle(\mathbf{x}) \simeq \frac{\sum_i^{N_t} \rho_i(\mathbf{x}) g_i(\mathbf{x})}{\sum_i^{N_t} \rho_i(\mathbf{x})}, \quad (12)$$

where N_t is the number of tetrahedra that intersect point \mathbf{x} . Note that g_i is only defined inside the corresponding tetrahedron i and is equal to zero outside. This is done most efficiently

by looping over all tetrahedra and adding their contributions to all the cells in the uniform grid whose cell centres are contained inside the tetrahedron. In fact, we subsample each cell 8 times, i.e. we compute the value for each cell by averaging over the values at 8 points inside the cell to arrive at a value closer to an actual volume average for each cell. We perform this operation for all points of a cubical lattice to obtain a three-dimensional data cube of velocity information.

3 SIMULATIONS

We have performed a series of cosmological simulations covering a considerable range in box sizes and mass resolutions to ensure convergence of our results. In all cases, we generated initial conditions using MUSIC (Hahn & Abel 2011) adopting the parametrisation of the transfer function of Eisenstein & Hu (1999) for the cold-dark matter (CDM) simulations as well as a truncated transfer function for the warm-dark matter (WDM) simulations that we detail below. We use cosmological parameters consistent with the WMAP7 data release (Komatsu et al. 2011). Specifically, we use the density parameters $\Omega_m = 0.276$, $\Omega_\Lambda = 0.724$ and $\Omega_b = 0.045$, a Hubble parameter of $h = 0.703$, power spectrum normalisation $\sigma_8 = 0.811$ and spectral index $n_s = 0.96$.

The initial conditions are generated by perturbing a regular lattice of particles using the Zel'dovich approximation at $z = 100$. The details on all the simulations that we use in this work are summarised in Table 1. All our analysis is performed at $z = 0$.

3.1 CDM simulations

For the CDM simulations, our four box sizes range between $3 h^{-1} \text{Gpc}$ and $100 h^{-1} \text{Mpc}$, the mass resolution is 512^3 particles in all cases, the $1 h^{-1} \text{Gpc}$ box has been also run at a higher resolution of 1024^3 particles. The gravitational evolution between $z = 100$ and $z = 0$ for these simulations has been performed using the tree-PM code L-GADGET 3 (Angulo et al. 2012) using a 1024^3 PM mesh for the simulations with 512^3 particles and a 2048^3 mesh for the simulations with 1024^3 particles. The softening adopted for the tree force is given in Table 1 for all cases.

3.2 WDM simulations

We consider also simulations starting from a perturbation spectrum with small-scale suppression in this work. This has the advantage that, unlike in CDM, the simulations are able to capture the full dynamic range of perturbations with enough resolution. We consider the same simulations as in Hahn et al. (2013), i.e., specifically, we adopt the parametrisation of the WDM transfer function from Bode et al. (2001) to modify the CDM transfer function

$$T_{\text{WDM}}(k) = T_{\text{CDM}}(k) [1 + (\alpha k)^2]^{-5.0}, \quad (13)$$

and

$$\frac{\alpha}{h^{-1} \text{Mpc}} \equiv 0.05 \left(\frac{\Omega_m}{0.4} \right)^{0.15} \left(\frac{h}{0.65} \right)^{1.3} \left(\frac{m_{\text{dm}}}{1 \text{keV}} \right)^{-1.15}, \quad (14)$$

which for the WDM particle mass of 300 eV equals a cut-off scale $\alpha = 0.21 h^{-1} \text{Mpc}$. For these simulations, we employed a modified version of GADGET-2 (Springel 2005) that uses only

Simulation Name	L_{box} $h^{-1}\text{Mpc}$	N_{p}	m_{p} $h^{-1}M_{\odot}$	ϵ $h^{-1}\text{kpc}$
L3000N512	3000	512^3	1.5×10^{13}	200
L1000N512	1000	512^3	5.7×10^{11}	65
L300N512	300	512^3	1.5×10^{10}	20
L100N512	100	512^3	5.7×10^8	6.5
L1000N1024	1000	1024^3	7.1×10^{10}	35
WDM512	40	512^3	3.7×10^7	78
WDM256	40	256^3	2.9×10^8	78
WDM128	40	128^3	2.3×10^9	78

Table 1. Labels and specifics of the simulations used in this work.

the particle-mesh force, evaluated on a 512^3 mesh (Note that we employ only the standard N -body simulations from Hahn et al. 2013 here). We simulated the gravitational evolution of one $40 h^{-1}\text{Mpc}$ box using 128^3 , 256^3 as well as 512^3 particles. The cut-off scale α is resolved in all three runs.

4 REAL-SPACE PROPERTIES OF THE COSMIC VELOCITY FIELD

In this section, we present the results of our analysis of velocity fields in real space. First, we show slices of the velocity divergence and vorticity in cosmological simulations of CDM and WDM structure formation. We then present their 1-point statistical properties and give a preliminary discussion of the velocity fields inside dark matter haloes.

4.1 Validation

We compare our results for velocity fields with corresponding results obtained with a Delaunay tessellation in Eulerian space, i.e. based on the particle positions only, which has been employed commonly in the literature (e.g. Icke & van de Weygaert 1987; Bernardeau & van de Weygaert 1996; Pueblas & Scoccimarro 2009; Jennings et al. 2011). Such a method does not involve a projection of the actual distribution function, but interpolates between the particles on the fine-grained distribution in configuration space (i.e. performs the tessellation after the projection) which necessarily leads to inconsistencies in multi-stream regions when the mesh on which the velocities are evaluated is of higher resolution than the Delaunay tessellation. We expect, however, this approach to perform better when the mesh cells are large and an effective coarse-graining is performed. As in our approach, velocities at an arbitrary point \mathbf{x} can be determined by linearly interpolating the velocity of the four vertices (particles) of the Delaunay tetrahedron containing \mathbf{x} to \mathbf{x} . To perform this calculation, we used the publicly available version 1.1.1 of DTFE¹ (Cautun & van de Weygaert 2011).

We have already discussed the difference between employing only configuration space information (such as DTFE) and using full phase space information in Section 2.5. Similar differences become readily visible when we inspect slices of the velocity field in one of the cosmological simulations. In the top panel of Fig. 4, we show the x -component of the velocity field for the L300N512 run. In the bottom panel, we show the respective velocity field obtained using DTFE. In both cases,

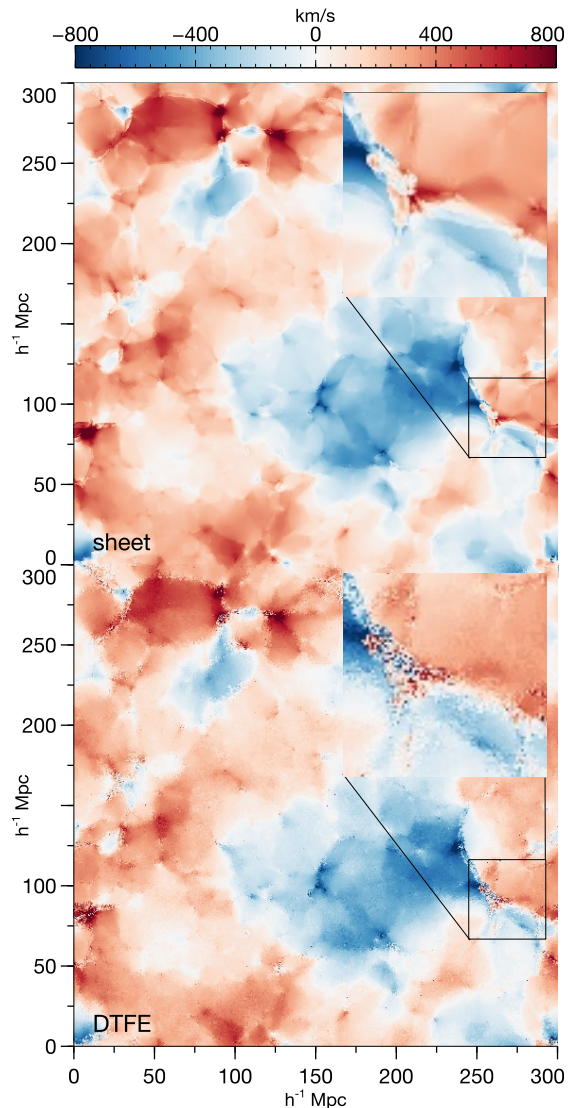


Figure 4. Slice of the cosmic velocity field from the L300N512 simulation obtained with the phase space tessellation method discussed in this work (top) and the DTFE method (bottom). Shown is the x -component of the velocity. The insets show enlargements of a $50 \times 50 h^{-2}\text{Mpc}^2$ region highlighting differences between the two methods in multi-stream regions. Equivalently to Fig. 1, noise in the lower panel inset arises due to interpolation between unrelated particles in the absence of phase-space information. Obtaining the correct point-wise mean-velocity field in multi-stream regions is only possible through a projection of the reconstructed fine-grained distribution function.

we have resampled to a cube of 512^3 cells. For the Delaunay tessellation, the small scale jitter due to linear interpolation between vertices that are not close in phase space and the lack of averaging in multi-stream regions is clearly apparent in the insets that zoom into the velocity field.

As discussed in Section 2.4, it is non-trivial to compute derivatives of the mean velocity field since a commutator between the derivative and the projection operator appears. We will illustrate this now by looking at slices of the velocity divergence field computed from the WDM512 simulation in Fig. 5 using various derivative estimators. Specifically, we compare the correct expression based on the fine-grained distribution function from eq. (7) (top left panel), with a divergence computed

¹ <http://www.astro.rug.nl/~voronoi/DTFE/dtfe.html>

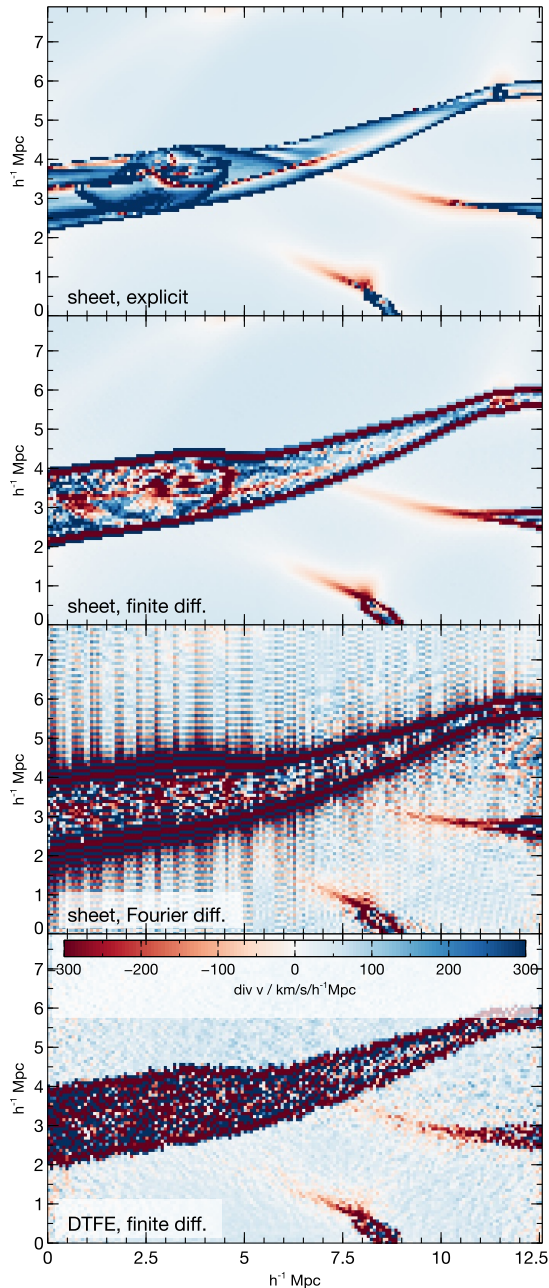


Figure 5. Slice of the velocity divergence field through a filament in the WDM512 simulation. We show results obtained with velocity fields computed using the dark matter sheet (top three panels) and using DTFE (bottom panel). The divergence is computed using the explicit divergence of the projected field from eq. (7) (top), 4th order finite differences on a mesh (second from top and bottom) as well as using spectral derivatives (third from top). See text for details.

on the gridded velocity field using a 4th order finite difference divergence operator (top right) and with the Fourier-space divergence operator (bottom left) that we will later employ when computing the spectral properties of velocity fields. The latter is given by computing $\text{div } \mathbf{v} = \mathcal{F}^{-1} [-i\mathbf{k} \cdot \mathcal{F}[\mathbf{v}]]$ using the fast Fourier transform (FFT) on the mesh on which we have computed the velocity field. Finally, we also show results when computing the velocity divergence for the DTFE estimate using again the 4th order finite difference operator. The differences for the velocity divergence fields computed using

the various methods are readily visible. As expected, computing derivatives on the noisier DTFE field leads to a noisy divergence field. The spectral derivative performs badly by producing Gibbs ringing due to the discontinuous field. Finally, we also clearly see that the finite difference estimate performs an implicit coarse-graining by differentiating on a finite scale across caustics leading to strongly compressive features on the infall side of every caustic, just as in the one-dimensional case that we have discussed above in Section 2.2. In fact, these compressive features, while depending on the scale on which the derivative is taken, are clearly the highest magnitudes of divergence compared to what is estimated away from caustics with eq. (7).

By using phase-space information to average over multi-stream regions, we thus expect that our method will greatly improve estimates of the true discontinuous nature of the velocity field and its derivatives on non-linear scales. With our approach it is possible to determine derivatives on significantly smaller scales than before, in fact even point-wise, without increasing the noise. We explore these aspects in more detail in the remainder of this paper.

4.2 Divergence and vorticity in CDM cosmic velocity fields

As we have discussed above and shown already in Fig. 5, pronounced differences in the real-space properties exist between divergence and vorticity estimated directly from the sheet and estimates based on finite differencing of the discontinuous velocity field.

In Fig. 6, we show slices through the CDM simulation L100N512, our simulation resolving the smallest scales. Specifically, we show the overdensity field (left panel), the velocity divergence (middle panels) as well as the vorticity field (right panels). Note that the colour map of the velocity divergence has been inverted with respect to that of the density field (also in the remainder of the paper), to allow for a more easy comparison in terms of the anti-correlation between the two fields in linear theory. Again, we show two versions of velocity derivative estimation, the sheet-based estimate following eqs. (7) and (8) in the top panels as well as a finite difference estimate in the bottom panels. All fields were sampled onto a cubical lattice of 512^3 cells and each slice corresponds to one slice of the data cube.

We recover for these CDM simulations the same qualitative differences in the velocity divergence fields as already discussed above for the plane-wave as well as the WDM case: finite differencing leads to filaments surrounded by envelopes of strong compression which are a result of the differentiation across the caustic on a finite scale (see Section 2.4). In the sheet-based estimates, the velocity field is almost everywhere expansive, aside from small filaments that have not shell-crossed yet. This results is not easily discernible using finite-difference estimates for the derivatives.

Similar differences resulting from the derivative estimation can be seen for the vorticity field. Applying eq. (8) leads to a vorticity that is explicitly zero in single-stream regions. The finite difference approach fails to recover this aspect. In addition, due to differentiation across caustics, a similar envelope of high vorticity is visible at caustics as the maxima of compression discussed above. We observe that, as discussed by Pichon & Bernardeau (1999), a jump in vorticity occurs at the

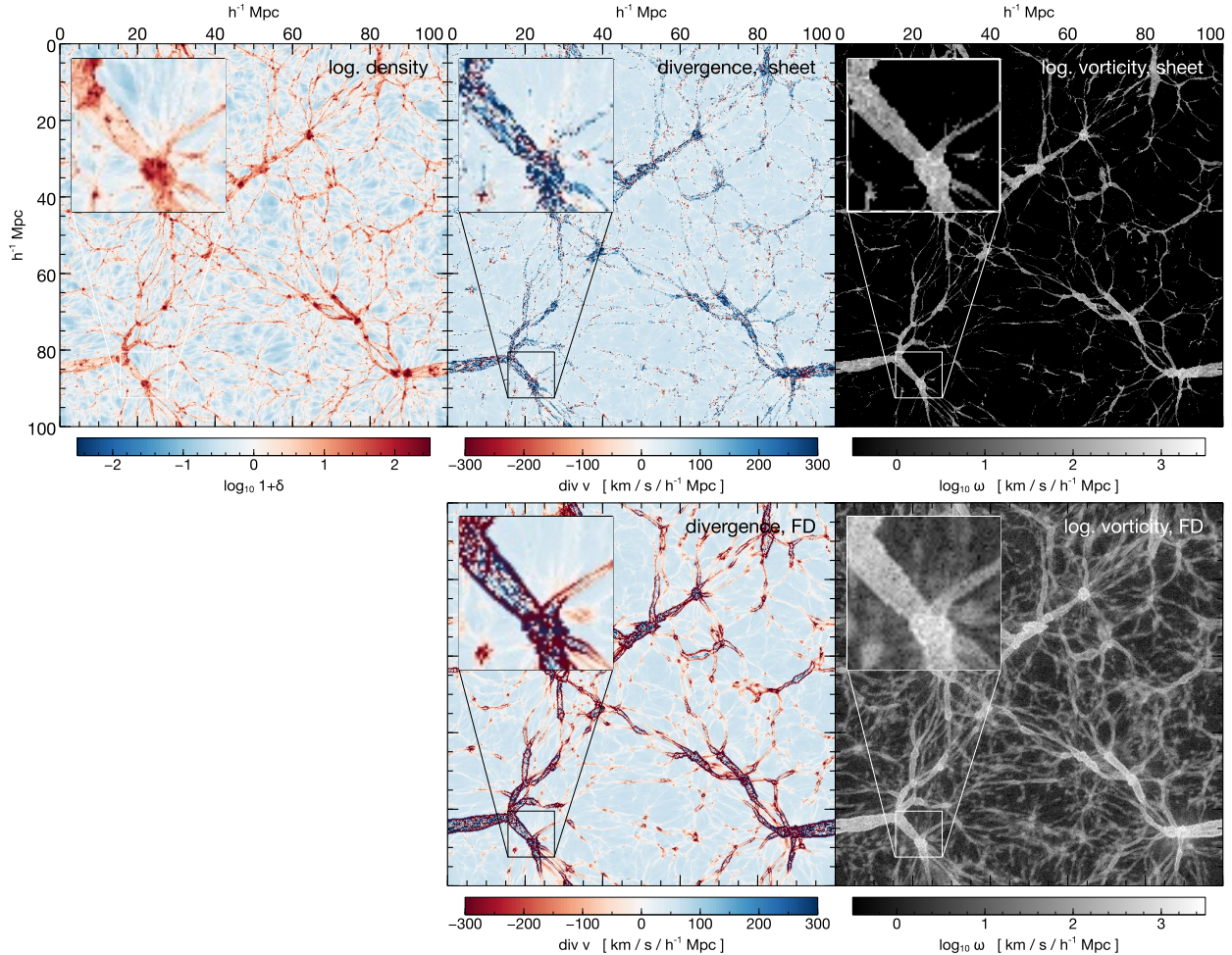


Figure 6. Slice through the overdensity (left panel), velocity divergence (middle panels) and the vorticity (right panels) fields of the L100N512 simulation. Divergence and vorticity in the top row have been calculated directly from the dark matter sheet using eqs. (7) and (8), while those in the bottom row have been calculated from velocity fields computed from the dark matter sheet for which divergence and vorticity were calculated using finite differences. Note that the vorticity is plotted logarithmically, while the velocity divergence (due to its changing sign) is not.

same locations as the caustics and with a similar magnitude in velocity change.

4.3 The velocity field in haloes

We continue our qualitative discussion of velocity fields by investigating in more detail the most massive halo of mass $M_h \sim 1.4 \times 10^{14} h^{-1} M_\odot$ (which corresponds to ~ 4 million particles) in our WDM512 simulation. We perform this analysis for the WDM case since the truncation of the perturbation spectrum allows us to resolve the collapse of those perturbations that are present with enough resolution. This cannot be achieved in the CDM case since perturbations up to the resolution limit exist.

In Fig. 7, we show slices of the density field (top left), velocity divergence (bottom left), the vorticity (top right) as well as the y -component of the vorticity vector field (bottom right) through the centre of this most massive halo. We now clearly see how the velocity divergence is positive in both void regions as well as predominantly positive in regions that have shell crossed. The only regions of *convergence* are given by

regions of moderate overdensity that are not yet shell-crossed (but will do so in the future and are visible in red colour in the divergence map and not visible in the vorticity magnitude maps in Fig. 7). This can be clearly seen from the vorticity slice, where the convergent regions are not visible, indicating that they have not yet shell-crossed. The vorticity increases with every caustic, being highest in the outer parts of the virialised regions of the halo. In the very centre of the halo, the velocity field is convergent and the vorticity decreases again.

We show these aspects in more details in Fig. 8, where we plot spherically averaged profiles of the density, vorticity, velocity divergence and the three tidal field eigenvalues. The density profile has not been calculated with the dark matter sheet, instead we simply plot the overdensity of N -body particles per shell to avoid the centrally biased profiles we have observed for the sheet in AHK12. The drop in vorticity and, more importantly, the sign reversal of the velocity divergence in the central region are now more clearly visible than in Fig. 7.

We observe a behaviour of the vorticity and divergence profiles that is consistent with our visual inspection of the slices. Velocity divergence rises as we enter the virial radius, is highest just inside the virial radius, then declines and becomes

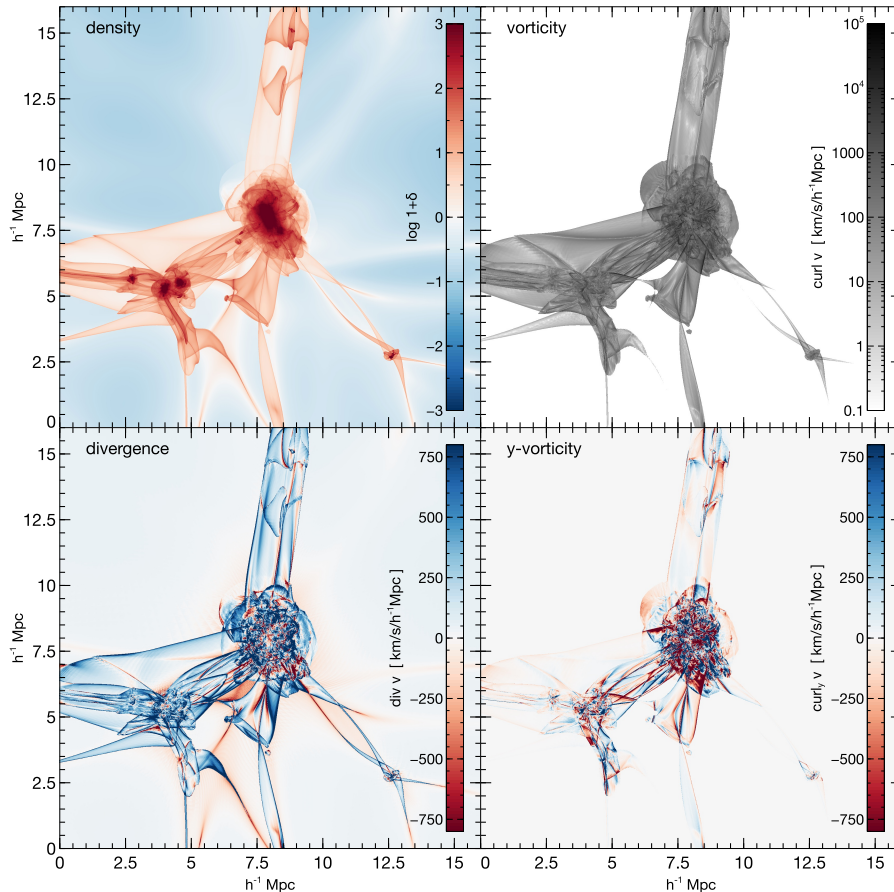


Figure 7. Slices through the centre of the most massive halo from the WDM512 simulation. **Top left:** overdensity field in logarithmic scale; **bottom left:** velocity divergence field, convergent flow is shown in blue, divergent in red; **top right:** the vorticity field in logarithmic scale; **bottom right:** y -component of the vorticity vector field in linear scale. The extent of each slice corresponds to $16 h^{-1} \text{Mpc}$, the slice itself is infinitesimally thin.

negative for $r \lesssim 0.2 h^{-1} \text{Mpc}$. This qualitative behaviour is present for both the divergence of the mean velocity field, as well as the averaged single stream divergence. We note that, at least for the halo we inspect, the radius where the divergence flips sign is close to the point where $\frac{d \log \delta}{d \log r} \sim 2$. In Appendix B, we show that while the details of the velocity divergence profiles converge rather slowly with increasing resolution, the qualitative features – i.e. the shape of the profile as well as the peak position and, most importantly, the radius at which the profile switches sign – are remarkably stable across resolutions.

One might thus speculate whether the change from convergent to divergent could be caused by a corresponding change of the tidal field. We also show the three eigenvalues of the tidal tensor in Fig. 8. The tidal field eigenvalues $\lambda_1 \leq \lambda_2 \leq \lambda_3$ are obtained by diagonalising the tidal field tensor $T_{ij} \equiv -\partial_i \partial_j \hat{\phi}$, where $\hat{\phi}$ is the gravitational potential normalised in such a way that $\text{tr} T_{ij} = \lambda_1 + \lambda_2 + \lambda_3 = -\delta$. We find that the eigenvalue signature is $(- - +)$ at all radii, implying one-dimensional stretching and two-dimensional compression. It thus seems not very plausible that the change from convergent to divergent flow is of a simple tidal origin. The associated drop in vorticity might point towards an isotropised inner region, where particle velocities are well aligned with density gradients. We only pointed out a few, rather qualitative, observations of the properties of mean velocity fields in haloes. A more rigorous

and detailed inspection is beyond the scope of this paper and will be followed up in future work.

4.4 One-point statistics

In this section, we return to the global statistics of the velocity field in cosmological volumes. In Fig. 9, we show the volume weighted probability distribution functions (PDFs) of the velocity divergence and vorticity fields. We find that the CDM vorticity PDFs that we show are reasonably well described by a lognormal distribution

$$p(\omega | \mu, \sigma) = \frac{1}{\sqrt{2\pi}\sigma\omega} \exp\left(-\frac{(\log \omega - \mu)^2}{2\sigma^2}\right), \quad (15)$$

with best fit parameters (μ, σ) of $(3.55, 1.3)$, $(3.42, 1.14)$ and $(3.45, 1.10)$ for L100N512, L300N512 and L1000N1024, respectively. Quite in contrast, the WDM vorticity distribution has a distinctly different shape with strongly enhanced wings and a change in slope at large vorticity. Similar behaviour can be observed in the PDFs of the velocity divergence. While the CDM distributions have power-law tails at both positively and negatively large values, the WDM distribution has a distinctly enhanced tail.

Most remarkably, *all* velocity divergence PDFs have a distinct feature, a bump just below $\text{div } \mathbf{v} \sim 70 \text{ km/s}/h^{-1} \text{Mpc}$. The origin of this feature becomes apparent when we plot the

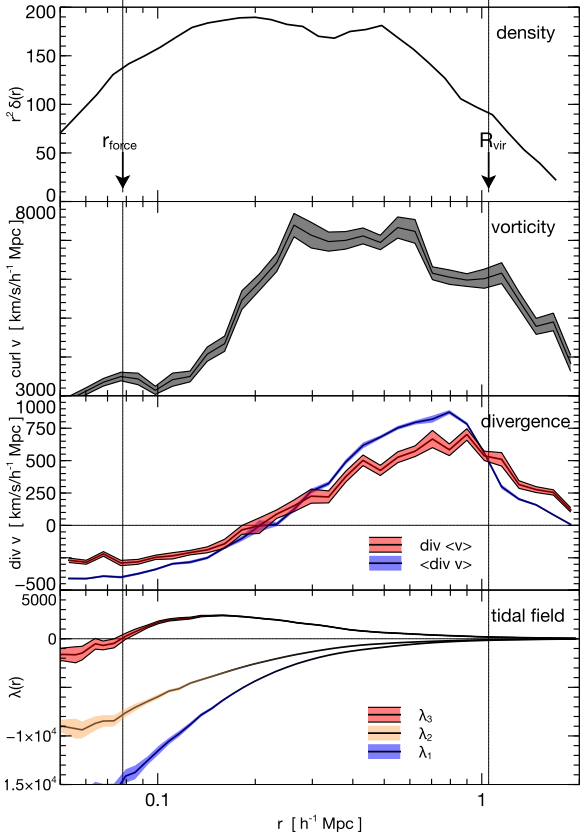


Figure 8. Halo profiles for the most massive halo in WDM512. Panels are, from top to bottom: the radial overdensity profile; the vorticity of the mean velocity field; divergence of the mean velocity field (red) and the average velocity divergence of single streams (blue); eigenvalues of the tidal tensor. Shaded regions show the median as well as the error on the median based on the 16th and 84th percentile. A convergence study of the velocity divergence is shown in Appendix B.

two dimensional distribution of overdensity-velocity divergence pairs. We show these, separately for the CDM simulation L100N512 and WDM512, in the left panel of Fig. 10. From this figure, and rather as expected, it is readily apparent that in underdense regions, a tight correlation between velocity divergence and overdensity exists. This correlation weakens with increasing density, and completely disappears for $\log_{10} 1 + \delta \gtrsim -0.5$ in the case of CDM, and for $\delta \gtrsim 0$ for WDM. In the WDM case, we observe a very sharp upper limit to the possible velocity divergence at a given underdensity. This limit can be easily understood, since the expansion rate $\theta_{\text{void}} \equiv H_0^{-1} \text{div } \mathbf{v}$ of a spherical void is directly related to its overdensity δ (which, of course, is in fact an underdensity) through the nonlinear equations (cf. Bernardeau et al. 1997; van de Weygaert & Bond 2008)

$$\theta_{\text{void}} = \frac{3 \Omega_m^{0.6} - \Omega_{\text{void}}^{0.6}}{2 \frac{1 + \Omega_{\text{void}}^{0.6}}{2}}; \quad \Omega_{\text{void}} = \frac{\Omega_m (1 + \delta)}{(1 + \theta_{\text{void}}/3)^2}. \quad (16)$$

We indicate the spherical void expansion rate by a dashed orange line in Fig. 10. It attains a maximum value of $\sim 69 \text{ km/s/h}^{-1} \text{ Mpc}$ for $\delta = -1$, which we show as the vertical line in Figure 9. In the CDM case, this does not in fact provide an upper limit but rather describes the median relation for $\delta \lesssim -0.5$ very well. This is plausibly simply due to the small-scale noise inherent to CDM simulations.

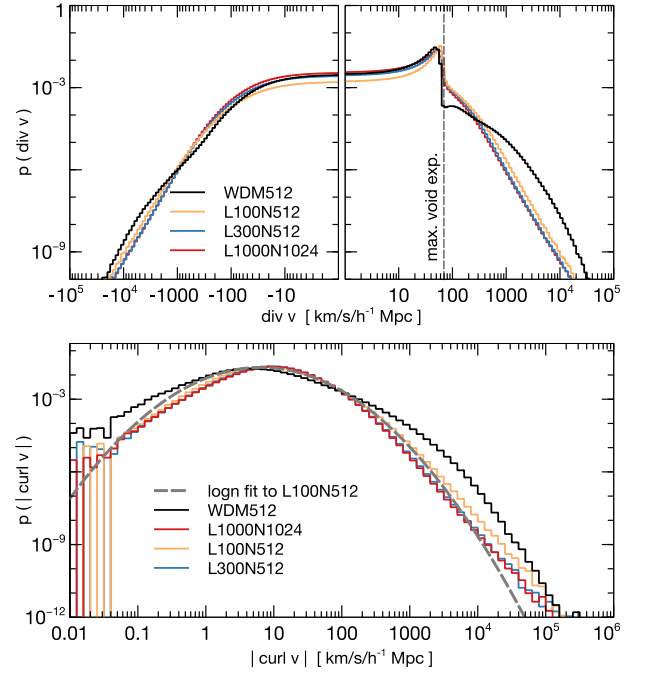


Figure 9. Volume weighted probability distribution functions of the velocity divergence (top) and vorticity (bottom) for various simulations. The vertical dashed black line in the top right panel indicates the maximum velocity divergence for a completely empty void (i.e. $\delta = -1$, for which $\text{div } \mathbf{v} = \frac{3}{2} \Omega_m^{0.6} H_0$). The dashed gray line in the bottom panel shows the reasonably good fit of a lognormal distribution to the vorticity PDF of simulation L100N512.

The apparent loss of the correlation at mean density seems to contradict the well known anti-correlation between density and velocity divergence that is exact in linear theory and not expected to break down so dramatically at mean density. The difference is, of course, that the exact formulae are point-wise and do *not* include the contribution of caustics. As discussed in Section 2.4, the discontinuous velocity jumps with associated singular derivative live on a subspace of measure zero and thus do not contribute to the volume-weighted one-point statistics without coarse-graining. Once we smooth our density and velocity fields on some scale so that the caustics are blurred out over a finite scale, we recover the expected result. In the right panel panel of Fig. 10, we thus show the density against the velocity divergence computed using finite differences from the sheet estimate of the mean velocity field. In contrast to the left panel, density and velocity divergence were smoothed with a Gaussian filter on a $1 h^{-1} \text{ Mpc}$ scale. This implies that ordinary differentiation can be applied since the discontinuities disappear. As expected, we recover the strong correlation that is expected between these two quantities even in the non-linear regime (cf. e.g. Bernardeau et al. 1999; Kudlicki et al. 2000). Interestingly, the correlation in the WDM simulation is significantly tighter, but it is plausible that the scatter is simply reduced due to the relatively small box size of that simulation.

Finally, we verify the global volume average of the divergence field. We note that $\langle \text{div } \mathbf{v} \rangle = 0$ (the angle brackets here denote a volume average) in the linear regime – due to Stokes’ theorem and periodic boundary conditions – and it is interesting to ask whether this holds in the non-linear regime as well, despite the markedly asymmetric PDFs that we found

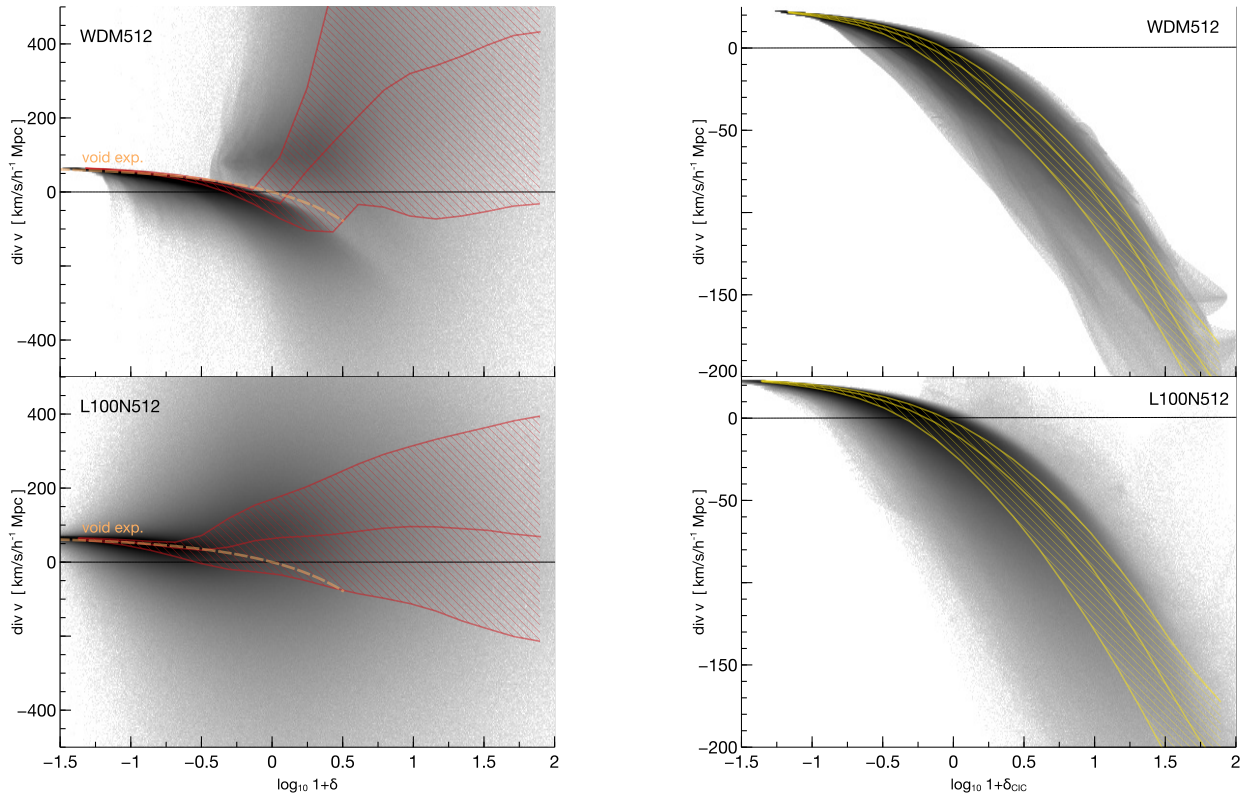


Figure 10. The correlation between velocity divergence and density. **Left Panel:** Here we show the point-wise velocity divergence and sheet density for the WDM512 simulation (top) and the L100N512 box (bottom). In the point-wise measurement, at low overdensities, a strong correlation exists that disappears around mean density. The red hatched area indicates the 16th and 84th percentile as well as the median in each bin of δ . The dashed orange line represents the velocity divergence of a spherical void of overdensity δ . **Right Panel:** The spatially averaged version of the left panel, where the density and the velocity divergence field were smoothed with a Gaussian kernel on $1 h^{-1} \text{Mpc}$ scales for the WDM512 simulation (top) and the L100N512 box (bottom). We observe the well-known strong anti-correlation between density and velocity divergence. The yellow lines indicate median and 16th and 84th percentile. See text for details.

above. First, for the divergence of the smoothed field this is true by definition, since in Fourier space the derivative operator is zero at $\mathbf{k} = 0$, implying a vanishing DC mode. Second, for the exact divergence estimated on the sheet, we can only compute this numerically. We find that for the WDM runs the volume averaged mean divergence is about 0.5 per cent of the standard deviation of the divergence, while for the highest resolution CDM run, i.e. L100N512, it is ~ 1.5 per cent and much smaller for the larger CDM boxes, i.e. overall consistent with a vanishing mean.

We thus arrive at a rather interesting conclusion. The big difference between the density–velocity divergence relation including jumps at caustics and excluding them demonstrates quite clearly that caustics with their compressive jumps dominate the velocity statistics in overdense regions when coarse graining is applied. On the other hand, if the compressive caustics are not included, the velocity field in overdense regions is predominantly of positive divergence, completely consistent with our discussion of the velocity field of the single halo in Section 4.3. Another interesting observation is that the maximum void expansion rate is not reached asymptotically in the smoothed statistics.

5 SPECTRAL PROPERTIES OF THE COSMIC VELOCITY FIELD

In this section, we present our main results regarding the *spectral* properties of cosmic velocity fields. We first outline fundamental differences between divergence and vorticity calculated in real and in Fourier space, before we will present power spectra of the velocity divergence and vorticity as well as density–divergence cross spectra for all our CDM and WDM simulations along with a convergence study and a comparison with results obtained with the DTFE.

5.1 Radial and transversal velocity modes vs. divergence and curl

The Fourier transform of the gradient operator ∇ is given by $-i\mathbf{k}$, so that in Fourier space the divergence and the curl of the velocity field \mathbf{v} become purely radial and transversal projections of the Fourier transformed velocity field:

$$\tilde{\theta} \equiv -i\mathbf{k} \cdot \tilde{\mathbf{v}} \quad (17)$$

$$\tilde{\omega} \equiv -i\mathbf{k} \times \tilde{\mathbf{v}}, \quad (18)$$

where the tilde denotes a Fourier transformed field, which we will omit in what follows.

We note that we do not use the divergence and curl computed using the sheet to study the spectral properties, but rather the velocity field itself and then perform the radial and

transversal projections. The reason for this is that a Fourier transform of the singular derivatives at the caustics needs to be performed as well, rather than just the field away from the caustics in order to obtain the correct spectra. This result can be easily seen from the definition of the Fourier transform:

$$\int_{\mathbb{R}} (v_r - v_l) \delta_D(x - x_0) \exp[-ikx] dx = (v_r - v_l) \exp[-ikx_0]. \quad (19)$$

One might be tempted to believe that only spectral derivatives should be used and derivatives on the tetrahedra should be avoided. While this is certainly warranted for the spectral properties of the velocity field, the inverse discrete Fourier transforms of the fields θ and ω have little to do with the divergence and curl of the mean velocity field. This is expected since the mean velocity fields are discontinuous and thus slowly decaying in Fourier space so that their Nyquist limited spectral derivatives are particularly ill behaved at the caustic locations where the derivative is infinite. We remind the reader of the comparison of divergence fields obtained with a spectral derivative, a 4th order accurate finite difference operator, as well as by using 1st order accurate finite differences on the tetrahedra with explicit evaluation of the derivative of the projected field (according to eq. 7) in Fig. 5.

5.2 Power spectra of the radial and transversal modes and the cross-spectrum with density – $P_{\theta\theta}$, $P_{\omega\omega}$ and $P_{\delta\theta}$

In what follows, we are concerned with the power spectrum of the radial $\theta(\mathbf{k})$ and transversal velocity modes $\omega(\mathbf{k})$ defined using spectral derivatives (see the discussion in Section 5.1). Their respective power spectra are given by

$$\langle \theta(\mathbf{k}) \theta^*(\mathbf{k}') \rangle = P_{\theta\theta}(k) \delta_D(\mathbf{k} - \mathbf{k}'), \quad (20)$$

$$\langle \omega(\mathbf{k}) \cdot \omega^*(\mathbf{k}') \rangle = P_{\omega\omega}(k) \delta_D(\mathbf{k} - \mathbf{k}'). \quad (21)$$

Cosmological initial conditions generated at arbitrary order of Lagrangian perturbation theory represent a purely potential flow before shell-crossing (see e.g. Bernardeau et al. 2002, for a review), i.e. $\mathbf{v} = \nabla\psi$, where ψ is the velocity potential at a given order of the perturbation theory. Hence, a Poisson equation exists for ψ of the form $\Delta\psi = 4\pi\theta$ and at linear order $\theta \propto -\delta$. However, at late times, vorticity is generated in the mean velocity field by multi-streaming, just as we have discussed in the first part of this paper.

It is thus interesting to consider the cross-spectrum between the overdensity δ and the velocity divergence θ , i.e.

$$\langle \theta(\mathbf{k}) \delta^*(\mathbf{k}') \rangle = P_{\theta\delta}(k) \delta(\mathbf{k} - \mathbf{k}'), \quad (22)$$

In linear perturbation theory, this is just a scaled version of the density power spectrum, but the growth of vorticity destroys the potential flow and transversal modes become important. We thus expect the cross-spectrum to drop rapidly at the scales where vorticity is generated and to reverse its sign on scales where shell-crossing has occurred, which is exactly what we will find below.

As we have discussed in AHK12 and Hahn et al. (2013), the density field estimated from the sheet is somewhat biased high in the densest regions (inner regions of haloes) since the sheet, linearly interpolated between particles, no longer tracks there the true distribution function. As we want to complement the velocity field analysis in this paper with an unbiased estimator, we resort to the noisy standard method of simple CIC deposit

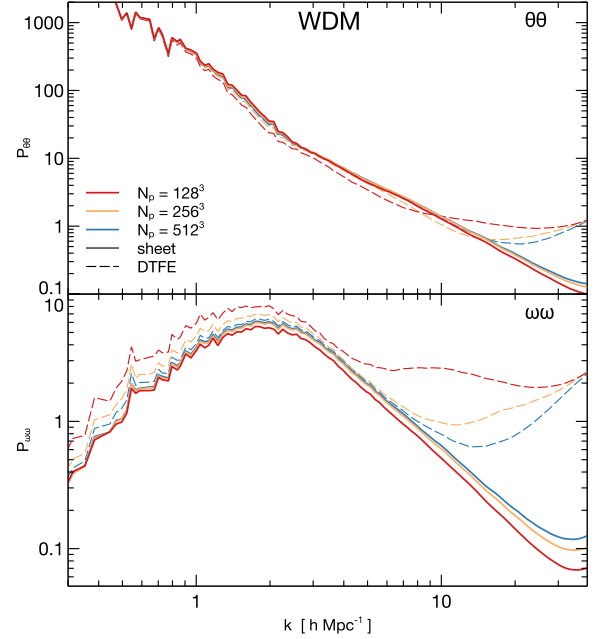


Figure 11. Power spectra at $z = 0$ of the divergence (top panel) and the vorticity (bottom panel) for the WDM simulations. All simulations used the same PM force resolution of 512^3 cells, but had varying mass resolution: 128^3 (red), 256^3 (yellow) and 512^3 (blue). Results obtained using the sheet tessellation are shown with a *solid line*, respective results obtained with DTFE are shown with *dashed lines*. While the two methods yield comparable results on large scales, only the sheet method shows convergence on small scales.

into the three-dimensional data cube (Hockney & Eastwood 1981). We then deconvolve with the CIC assignment kernel to correct the suppression of small-scale power close to the grid Nyquist wave number. Specifically, we deconvolve with the kernel

$$W_{\text{CIC}}(\mathbf{k}) = \prod_{i=x,y,z} \left(\frac{\sin \pi k_i / 2k_{\text{Ny}}}{\pi k_i / 2k_{\text{Ny}}} \right)^2$$

before computing the power spectrum of the overdensity field δ by evaluating

$$\langle \delta(\mathbf{k}) \delta^*(\mathbf{k}') \rangle = P_{\delta\delta}(k) \delta_D(\mathbf{k} - \mathbf{k}'). \quad (23)$$

We compute all spectra by performing a fast Fourier transformation of the three-dimensional data cube of the respective quantities followed by computing binned averages of all modes that fall into logarithmically spaced intervals $k_j \leq k \leq k_{j+1}$.

5.3 Velocity divergence and vorticity power spectra for WDM

We first investigate the velocity divergence and vorticity power spectra for our WDM simulations, which all have the same PM force resolution but have varying mass resolution. The 300 eV initial WDM power spectrum leads to a truncation of perturbations that is resolved in all simulations (see also the discussion in Angulo et al. 2013). At fixed force resolution this should mean that one can arrive at perfectly converged properties. This is in stark contrast to the CDM case that we will discuss below, where more perturbations are introduced when the mass resolution is increased since the perturbation

spectrum of CDM continues to almost arbitrarily small scales (see also our discussion of this in AHK12 and Hahn et al. 2013)

For this reason, we expect to achieve actual convergence if the simulation resolves both the cut-off scale and the non-linear scale. We thus re-analyse the simulations introduced in Hahn et al. (2013) for a toy model 300 eV WDM particle. We do not use the simulation outputs obtained with the new simulation technique introduced in that paper, but make use of the standard PM results in order to keep the discussion purely focused on the analysis of the simulation data rather than the simulation technique.

We show the divergence and vorticity power spectra for our three WDM runs in Fig. 11, comparing again with DTFE. It is quite remarkable that the divergence spectra determined using the sheet are converged irrespective of resolution at all $k \lesssim 10 h/\text{Mpc}$ with very small discrepancy at larger k . The vorticity spectra show a small resolution dependence in amplitude, increasingly so at larger k , but not in shape. For the divergence spectra obtained with DTFE, we observe slower convergence, in particular scales $k \gtrsim 3 h/\text{Mpc}$ show a very strong dependence on the mass resolution. Even more pronounced is the lack of convergence for the vorticity spectra. Here, in the case of DTFE, all scales show a resolution dependence, unlike for the sheet estimated vorticity which is perfectly converged on small scales. In addition, for DTFE, at small scales, the vorticity spectra appear to converge slowly to a power-law with positive index. This is most likely due to the lack of an actual projection of the distribution function in this approach, where the single particle velocity dispersion becomes sampled in multi-stream regions rather than the mean velocity. These results are a particularly good example of the strength of our phase-space based estimate of cosmic velocity fields. A remarkable difference is that the phase space sheet estimate of the vorticity spectrum converges from below, while the DTFE estimate converges from above.

5.4 Results: Power spectra of the velocity and density field for CDM

In Fig. 12, we present, for all 5 CDM simulations, the velocity divergence (top panel), and vorticity (second from top panel) power spectra, as well as the density-velocity divergence cross spectrum (third panel from top) and the density power spectrum (bottom panel). Our results are largely consistent with results of Pueblas & Scoccimarro (2009). In particular, we observe as well that converged power spectra require that the non-linear scale is well resolved. Pueblas & Scoccimarro (2009) observe that a mass resolution below $10^9 h^{-1} M_\odot$ is necessary at $z = 0$ for converged spectra, consistent with our results. Both, the results of these authors as well as ours indicate that this is mostly due to the slow convergence of the flow vorticity. Somewhat unexpectedly however, Pueblas & Scoccimarro (2009) do not find an obvious resolution dependence of the convergence spectrum (while they do for the vorticity spectrum).

Since vorticity is driven by small-scale non-linearities, we find that the slow convergence of vorticity is, at least to some degree, driven by a lack of resolution at the non-linear scale: when running the L1000N512 box with a force resolution of only 8 times the mean inter-particle distance we observe a significant drop of the large-scale vorticity spectrum (not shown).

We next discuss the differences we see in spectra estimated using the phase space sheet compared to a standard Delaunay tessellation approach. In Figure 13, we compare the divergence and vorticity spectra computed from the velocity field estimates

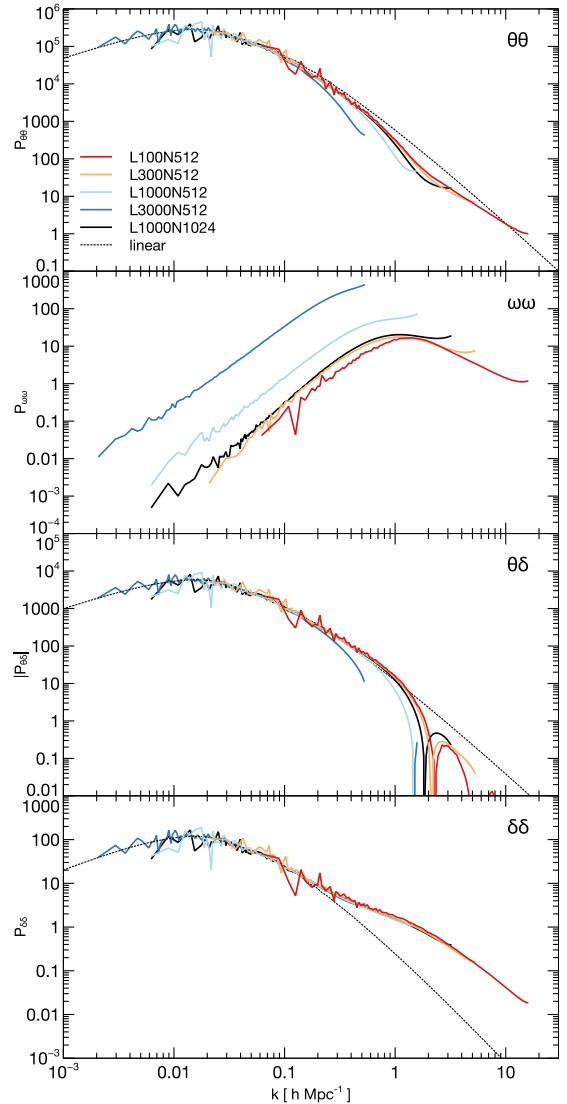


Figure 12. Power spectra of the velocity divergence (top panel), vorticity (second from top), the cross spectrum between velocity divergence and overdensity (third from top) and the density power spectrum (bottom). Data is given for all the simulations we performed, indicated by the different colors. The spectra predicted by linear perturbation theory are given by the dotted lines, the prediction for the vorticity spectrum is zero.

based on the dark matter sheet with those obtained using the DTFE. We perform this comparison only for the three simulations L100N512, L300N512 and L1000N512. For the divergence spectrum, we observe that (1) all spectra, from DTFE and sheet, converge to the same spectrum with increasing small scale resolution, (2) the DTFE spectra show a pronounced rise at the smallest scales which is due to the small scale noise discussed above in Section 4.2, (3) convergence at all scales is faster for the sheet-based estimates than for the DTFE-based estimates. For the vorticity spectra, which are clearly the most challenging to estimate reliably, an essentially identical picture emerges but convergence is considerably slower with increasing resolution for DTFE than for the sheet based estimate.

In Fig. 14, we show the slope of the vorticity power spectrum $n_\omega \equiv d \log P_{\omega\omega} / d \log k$ as a function of wavenumber k . We find that $n_\omega \rightarrow 5/2$ on large scales for $k \lesssim 0.1 h \text{ Mpc}^{-1}$

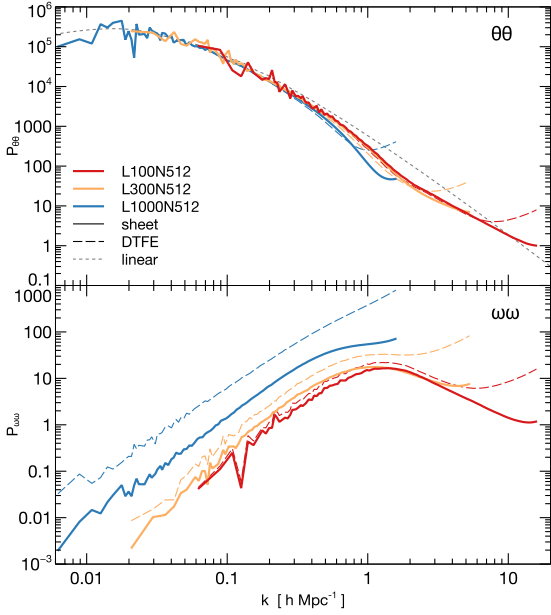


Figure 13. Power spectra at $z = 0$ of the divergence (top panel) and the vorticity (bottom panel) of the $1 h^{-1}\text{Gpc}$ (red), $300 h^{-1}\text{Mpc}$ (yellow) and $100 h^{-1}\text{Mpc}$ (blue) boxes with 512^3 particles in each case. Results obtained using the sheet tessellation are shown with a solid line, respective results obtained with DTFE are shown with dashed lines.

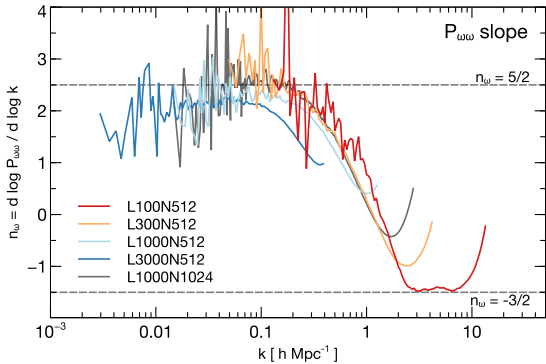


Figure 14. Slope of the vorticity power spectrum $P_{\omega\omega}$ at $z = 0$ showing an asymptotic behaviour consistent with $P_{\omega\omega} \propto k^{5/2}$ for small k and $P_{\omega\omega} \propto k^{-3/2}$ for large k .

(consistent with the predictions of Carrasco et al. 2014) and $n_{\omega} \rightarrow -3/2$ on small scales for $k \gtrsim 1 h \text{Mpc}^{-1}$. The simulations that have the lowest mass resolution, notably L1000N512 and L3000N512, already showed a spurious significantly enhanced vorticity amplitude, also have a slightly lower n_{ω} on large scales. Unfortunately, only our simulation with the highest mass resolution demonstrates the asymptotic behaviour of the vorticity on small scales so that we cannot establish convergence of this value. This requires further investigation with higher resolution simulations to robustly measure the small-scale asymptotic slope.

5.5 Fitting formulae

In this section, we determine fitting functions for the bias of the velocity divergence relative to the matter density field for

$k < 1 h \text{Mpc}^{-1}$. This divergence bias b_{θ} can be defined either through the density–velocity divergence cross spectrum as

$$b_{\theta}^{(1)} = -\frac{1}{\mathcal{H}f} \frac{P_{\delta\theta}}{P_{\delta\delta}} \quad (24)$$

or through the velocity divergence power spectrum as

$$b_{\theta}^{(2)} = \frac{1}{\mathcal{H}f} \sqrt{\frac{P_{\theta\theta}}{P_{\delta\delta}}}, \quad (25)$$

where $\mathcal{H}f \equiv d \log D / d \log \tau$ and $D(\tau)$ is the linear growth factor. We find that both are well fit for $k \lesssim 1 h \text{Mpc}^{-1}$ by the exponential function

$$b_{\theta}(k) = \exp \left[- (k/\alpha)^{\beta} \right]. \quad (26)$$

We determine the fit parameters α and β by combining the spectra of the three boxes L100N512, L300N512 and L1000N512 for $k < 1 h \text{Mpc}^{-1}$. The divergence bias calculated from eq. (24) is shown in Fig. 15 (top panel, left) for the three boxes, the one calculated from eq. (25) in the top panel, right. When fitting the bias from the cross-spectrum, we find best fitting parameters $\alpha = 0.606 \pm 0.004 h \text{Mpc}^{-1}$ and $\beta = 1.176 \pm 0.017$. When fitting from the power spectrum, the best fit parameters are $\alpha = 0.7423 \pm 0.006 h \text{Mpc}^{-1}$ and $\beta = 1.112 \pm 0.018$. The relative error with respect to the fits is shown in the bottom panels of Fig. 15. We find that for $k \lesssim 1 h \text{Mpc}^{-1}$, the fits describe the data with about 5 per cent accuracy or better on larger scales. For a linear bias in the absence of noise, the two bias determinations should yield the same answer, but we find that this is only approximately true. Particularly, the parameter α implies a cut-off at slightly larger scales for the bias calculated from the cross-spectrum. We note that the density fields, obtained with CIC deposits, contain a shot-noise term that we have not subtracted. The level of agreement between the different simulations (with different amplitudes of shot-noise) implies however that the discrepancy between the two biases cannot be explained by shot-noise alone. The difference between the fits is thus plausibly caused by either a non-linear relation between density and velocity-divergence or another more complicated additive noise component. The difference between the fits could in part be due to a more complicated additive noise component, but most likely reflects the different scale-dependence of the non-linearities in density and velocity divergence (see Cieliegl & Chodorowski 2004, who find that $b_1(k)/b_2(k)$ is monotonically decreasing).

6 SUMMARY AND CONCLUSIONS

In this paper, we have extended the phase-space sheet tessellation method introduced in AHK12 to estimate the properties of volume-weighted cosmic velocity fields and their differentials, explicitly, the velocity divergence and vorticity. To our knowledge, this method is the only one that is able to take into account the discontinuous and multi-valued nature of the velocity field in multi-stream regions that arise wherever structures collapse gravitationally.

Even DTFE, which so far has been perhaps the best velocity estimator for numerical simulations, is plagued by noise in multi-stream regions and shows convergence relatively slowly for all properties of the velocity field. This can naturally be circumvented by our method, without the need of filtering on relatively large-scales at the expense of losing detailed features.

We can summarise the advantages of our approach as follows:

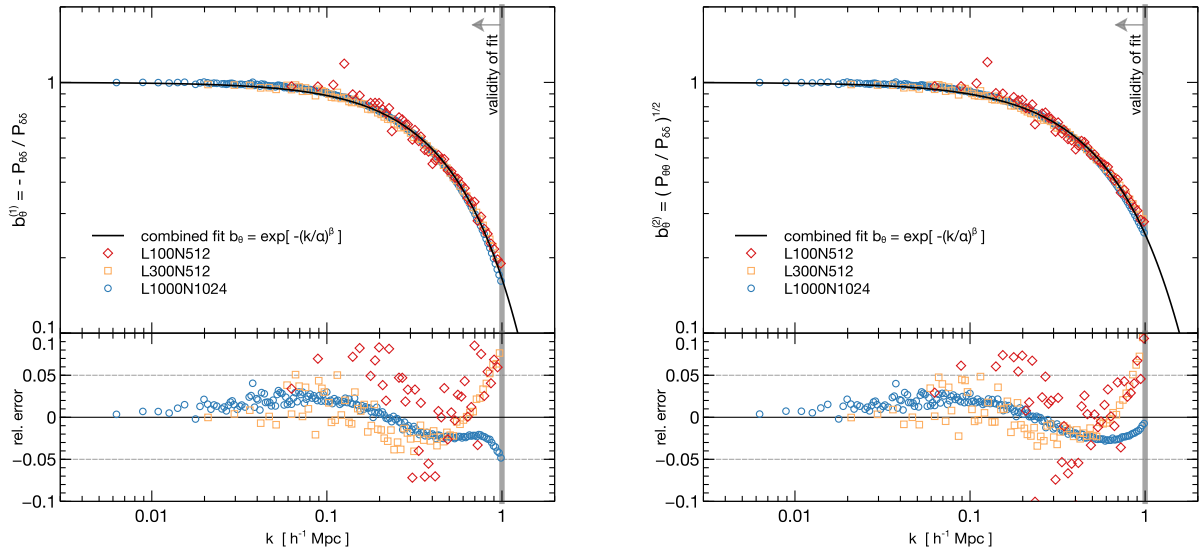


Figure 15. Fit of the divergence bias b_θ from the divergence-density cross spectrum (left panel) and from the divergence power spectrum (right panel) at $z = 0$ with an exponential function $b_\theta(k) = \exp[-(k/\alpha)^\beta]$ with best fitting parameters $\alpha = 0.606 \pm 0.004 h \text{ Mpc}^{-1}$ and $\beta = 1.176 \pm 0.017$ when estimated from the cross spectrum (left), as well as $\alpha = 0.7423 \pm 0.006 h \text{ Mpc}^{-1}$ and $\beta = 1.112 \pm 0.018$ when estimated from the divergence power spectrum (right). The vertical grey line indicates $k = 1 h \text{ Mpc}^{-1}$, the wave number up to which our fit was performed and is valid with an accuracy of about 5 per cent. At even larger k , b_θ changes its sign (see Fig. 12).

- (i) The phase space sheet allows a proper definition of a projection operator from phase space onto configuration space and thus properly averaged velocity fields in multi-stream regions. An estimate that does not respect the phase-space connectivity leads to small-scale jitter by interpolating between velocities that are close in configuration space but not close in phase space. Using the correct phase-space connectivity significantly reduces small-scale noise in the velocity fields.
- (ii) We derived exact expressions for the divergence and curl of the mean velocity field in multi-stream regions, eqs. (7) and (8), that explicitly do not include the discontinuities of the velocity field at caustics in multi-stream regions where derivatives are singular.
- (iii) By excluding the singular derivatives (which occupy a volume of measure zero), our technique can compute the differential properties of the mean velocity field without coarse-graining and thus the introduction of an arbitrary scale. By doing so, the differentials represent only the mean dynamics of the dark matter fluid instead of including also the motion of the singular caustics.

Thus, in summary, we find that our new method provides significantly improved estimates of cosmic velocity fields and their differential properties: it allows a proper definition of a phase-space projection operator that significantly reduces small-scale noise.

We applied this estimator to a set of cold and warm dark matter N-body simulations. We discussed in detail the differences that arise when ordinary finite differencing schemes and spectral derivatives are used. We showed that those operators perform an implicit coarse graining that includes the singular derivatives. We also presented an in-depth discussion of the real-space properties of the velocity field and its differential properties both in CDM and WDM. In the final part of the paper we focused on the spectral properties.

Our science results can be summarised as:

- (i) We demonstrated explicitly that the mapping between density and velocity divergence, i.e. $\text{div } \mathbf{v} \propto -\delta$, which holds in linear perturbation theory, appears as a strong correlation before shell crossing. After shell-crossing, the correlation reverses its sign. In shell-crossed regions, the only locations of predominantly negative divergence are the very centres of filaments and haloes. This implies that in overdense regions, the coarse-grained non-linear density-velocity anti-correlation is predominantly driven by the compressive caustics.
- (ii) Our results from WDM simulations indicate that, inside of haloes, the spherically averaged vorticity drops sharply and the velocity divergence changes its sign around the location where the density profile has a slope of -2 . The outer regions of the halo have a positive divergence, while the inner regions are convergent. This tentative result certainly warrants further investigation.
- (iii) We discussed the 1-point statistics of the divergence and vorticity fields and found that the divergence PDF exhibits a pronounced feature at the maximum void expansion rate. The vorticity PDF is reasonably well fit by a lognormal distribution. Furthermore, the two-dimensional histogram of overdensity vs. velocity divergence shows that for CDM the correlation between overdensity and velocity divergence is well described by the void expansion rate for $\delta \lesssim -0.7$ while for WDM, the void expansion rate provides a sharp upper limit to the velocity divergence at a given overdensity for $\delta \lesssim -0.7$.
- (iv) Velocity spectra for CDM obtained with the phase space sheet show faster convergence behaviour with resolution, but both our method and DTFE converge to the same spectra when the non-linear scale is very well resolved. Consistent with previous results, we find that the vorticity spectra require higher resolution in order to be converged than divergence spectra.

- (v) We complemented our discussion of spectral properties with an analysis of WDM simulations, where the entire perturbation spectrum can be resolved. Here, we are able to estimate spectra that are almost independent of the resolution of the underlying simulation, while the estimate on the position-space tessellation shows only slow convergence with resolution, is dominated by small scale noise and lacks convergence to the correct spectrum at small scales.
- (vi) Finally, we provided fits for a bias parameter b_θ in terms of a function exponentially decaying in wave number k that allows the CDM divergence power spectrum $P_{\theta\theta}$ as well as the divergence–overdensity cross spectrum $P_{\theta\delta}$ to be related to the non-linear matter power spectrum $P_{\delta\delta}$.

It will be interesting to follow up this preliminary analysis by probing the effect of cosmic large-scale velocity fields on the assembly of haloes and thus the alignment of their spins with larger scales as well as the connection between velocity fields and gravitational tidal fields (c.f. Aragón-Calvo et al. 2007; Hahn et al. 2007,?; Hoffman et al. 2012; Libeskind et al. 2013; Laigle et al. 2015). Another application of our method is to more reliably measure the “effective field” properties of dark matter (e.g. Carrasco et al. 2012). Future work should also study the second moment of the projected velocity field, i.e. the anisotropic stress tensor, in addition to the properties of the mean field.

ACKNOWLEDGEMENTS

O.H. thanks Aseem Paranjape for many fruitful discussions. The authors thank him as well as Stéphane Colombi and Christophe Pichon for valuable comments on the draft of this article. O.H. acknowledges support from the Swiss National Science Foundation (SNSF) through the Ambizione fellowship. We are grateful to Rien van de Weygaert and Marius Cautun for making the DTFE software publicly available. We gratefully acknowledge the support of Stuart Marshall and the SLAC computational team, as well as usage of the computational resources at SLAC and ETH Zurich. We thank our referee Michal Chodorowski for his very valuable comments that helped to improve the presentation of this paper.

REFERENCES

- Abel T., Hahn O., Kaehler R., 2012, **AHK12**, MNRAS, 427, 61
- Angulo R. E., Hahn O., Abel T., 2013, MNRAS, 434, 3337
- Angulo R. E., Springel V., White S. D. M., Cole S., Jenkins A., Baugh C. M., Frenk C. S., 2012, MNRAS, 425, 2722
- Angulo R. E., Springel V., White S. D. M., Jenkins A., Baugh C. M., Frenk C. S., 2012, MNRAS, 426, 2046
- Aragón-Calvo M. A., van de Weygaert R., Jones B. J. T., van der Hulst J. M., 2007, ApJ, 655, L5
- Ascasibar Y., 2010, Computer Physics Communications, 181, 1438
- Bernardeau F., Chodorowski M. J., Lokas E. L., Stompor R., Kudlicki A., 1999, MNRAS, 309, 543
- Bernardeau F., Colombi S., Gaztañaga E., Scoccimarro R., 2002, Phys. Rep., 367, 1
- Bernardeau F., van de Weygaert R., 1996, MNRAS, 279, 693
- Bernardeau F., van de Weygaert R., Hivon E., Bouchet F. R., 1997, MNRAS, 290, 566
- Bertschinger E., Dekel A., 1989, ApJ, 336, L5
- Bode P., Ostriker J. P., Turok N., 2001, ApJ, 556, 93
- Buchert T., 1992, MNRAS, 254, 729
- Carrasco J. J. M., Foreman S., Green D., Senatore L., 2014, J. Cosmology Astropart. Phys., 7, 57
- Carrasco J. J. M., Hertzberg M. P., Senatore L., 2012, Journal of High Energy Physics, 9, 82
- Cautun M. C., van de Weygaert R., 2011, arXiv:1105.0370
- Ciecielg P., Chodorowski M. J., 2004, MNRAS, 349, 945
- Colombi S., Chodorowski M. J., Teyssier R., 2007, MNRAS, 375, 348
- Dekel A., 1994, ARA&A, 32, 371
- Efstathiou G., Davis M., White S. D. M., Frenk C. S., 1985, ApJS, 57, 241
- Eisenstein D. J., Hu W., 1999, ApJ, 511, 5
- Hahn O., Abel T., 2011, MNRAS, 415, 2101
- Hahn O., Abel T., Kaehler R., 2013, MNRAS, 434, 1171
- Hahn O., Carollo C. M., Porciani C., Dekel A., 2007, MNRAS, 381, 41
- Hahn O., Porciani C., Carollo C. M., Dekel A., 2007, MNRAS, 375, 489
- Henon M., 1982, A&A, 114, 211
- Hockney R. W., Eastwood J. W., 1981, Computer Simulation Using Particles. McGraw-Hill
- Hoffman Y., Metuki O., Yepes G., Gottlöber S., Forero-Romero J. E., Libeskind N. I., Knebe A., 2012, MNRAS, 425, 2049
- Icke V., van de Weygaert R., 1987, A&A, 184, 16
- Jennings E., 2012, MNRAS, 427, L25
- Jennings E., Baugh C. M., Pascoli S., 2011, MNRAS, 410, 2081
- Kitaura F.-S., Angulo R. E., Hoffman Y., Gottlöber S., 2012, MNRAS, 425, 2422
- Komatsu E., Smith K. M., Dunkley e. a., 2011, ApJS, 192, 18
- Kudlicki A., Chodorowski M., Plewa T., Różycka M., 2000, MNRAS, 316, 464
- Laigle C., Pichon C., Codis S., Dubois Y., Le Borgne D., Pogosyan D., Devriendt J., Peirani S., Prunet S., Rouberol S., Slyz A., Sousbie T., 2015, MNRAS, 446, 2744
- Libeskind N. I., Hoffman Y., Steinmetz M., Gottlöber S., Knebe A., Hess S., 2013, ApJ, 766, L15
- Melott A. L., 1982, Physical Review Letters, 48, 894
- Melott A. L., Shandarin S. F., 1993, ApJ, 410, 469
- Monaghan J. J., 1992, ARA&A, 30, 543
- Pandey B., White S. D. M., Springel V., Angulo R. E., 2013, MNRAS, 435, 2968
- Peebles P. J. E., 1980, The large-scale structure of the universe. Princeton University Press
- Peebles P. J. E., Melott A. L., Holmes M. R., Jiang L. R., 1989, ApJ, 345, 108
- Pelupessy F. I., Schaap W. E., van de Weygaert R., 2003, A&A, 403, 389
- Pichon C., Bernardeau F., 1999, A&A, 343, 663
- Pueblas S., Scoccimarro R., 2009, Phys. Rev. D, 80, 043504
- Pumir A., Bodenschatz E., Xu H., 2013, Physics of Fluids, 25, 035101
- Schaap W. E., 2007, PhD thesis, Kapteyn Astronomical Institute
- Schaap W. E., van de Weygaert R., 2000, A&A, 363, L29
- Shandarin S., Habib S., Heitmann K., 2012, Phys. Rev. D, 85, 083005
- Sharma S., Steinmetz M., 2006, MNRAS, 373, 1293
- Springel V., 2005, MNRAS, 364, 1105

van de Weygaert R., Bond J. R., 2008, in Plionis M., López-Cruz O., Hughes D., eds, *A Pan-Chromatic View of Clusters of Galaxies and the Large-Scale Structure* Vol. 740 of *Lecture Notes in Physics*, Berlin Springer Verlag, Observations and Morphology of the Cosmic Web. p. 409

Wang X., Szalay A., Aragón-Calvo M. A., Neyrinck M. C., Eyink G. L., 2014, *ApJ*, 793, 58

APPENDIX A: DERIVATION OF THE VELOCITY DIVERGENCE AND CURL IN MULTI-STREAM REGIONS

We briefly derive here the expressions $\text{div} \langle \mathbf{v} \rangle$ as given in eq. (7) and $\text{curl} \langle \mathbf{v} \rangle$ as given in eq. (8). This is achieved by applying the derivative operator to the multi-stream average as given on the right-hand-side of eq. (3). Unlike in the main text, we write the stream index s as a superscript in order to distinguish it more clearly from Cartesian indices which are written as subscripts. We first note that in order for the derivative to commute with the sum over streams, \sum_s , the number of streams is not allowed to change in the point where the derivative is taken. Then $\partial_i \sum_s x^s = \sum_s \partial_i x^s$. This is only the case at caustics which is the reason for excluding them from the derivatives and consider them separately in Section 2.4. So, away from caustics, we now evaluate the mixed derivative $\partial_i \langle v_j \rangle$ from which divergence and curl can be constructed. We then have

$$\begin{aligned} \partial_i \langle v_j \rangle &= \partial_i \frac{\sum_s \rho^s v_j^s}{\sum_s \rho^s} \\ &= \frac{\sum_s (v_j^s \partial_i \rho^s + \rho^s \partial_i v_j^s)}{\sum_s \rho^s} - \frac{(\sum_s \rho^s v_j^s) (\sum_s \partial_i \rho^s)}{(\sum_s \rho^s)^2} \\ &= \frac{\sum_s v_j^s \rho^s \partial_i \log \rho^s}{\sum_s \rho^s} + \langle \partial_i v_j \rangle - \langle v_j \rangle \langle \partial_i \log \rho \rangle \\ &= \langle (\partial_i \log \rho) (v_j - \langle v_j \rangle) \rangle + \langle \partial_i v_j \rangle, \end{aligned} \quad (\text{A1})$$

where we have exploited various times the definition of stream averages $\langle x \rangle = (\sum_s x^s \rho^s) / \sum_s \rho^s$ and the idempotence of this average $\langle \langle x \rangle \rangle = \langle x \rangle$. The expressions for divergence and curl follow straightforwardly from the tensorial derivative (A1).

APPENDIX B: RESOLUTION STUDY OF THE VELOCITY FIELD IN HALOES

In this appendix, we assess the degree of convergence of the velocity fields estimated from the dark-matter sheet inside of virialized structures. We show a close-up version of the most massive halo in the WDM simulations in Fig. B1, to be compared to the respective panels of Fig. 7. We observe that the larger scale structures in the density field are remarkably stable with increasing resolution. Convergence in the velocity divergence field is however considerably slower.

We complement this rather qualitative comparison with radial velocity divergence profiles of the averaged single-stream velocity divergence in Fig. B2. Consistent with the slices discussed above, the qualitative features are stable across resolutions. While the velocity divergence profile is not yet converged, the peak location as well as the location of sign flip are consistent among the different resolutions.

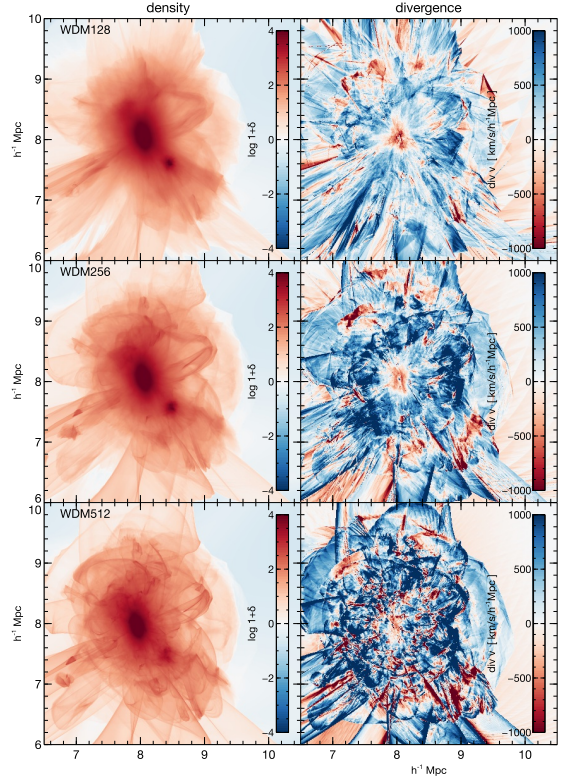


Figure B1. Convergence study of slices of the dark-matter sheet estimated density field and velocity divergence through the centre of the most massive halo of the WDM simulations. The bottom row panels are a close-up version of the corresponding panels in Fig. 7.

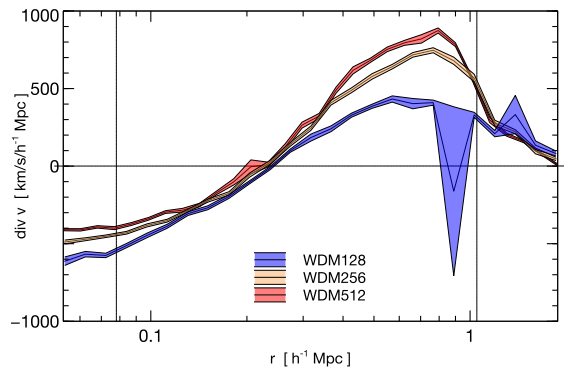


Figure B2. Convergence study of the spherically averaged single stream velocity divergence. Profiles are shown for all WDM simulations. While the peak properties have not yet converged, the point where the velocity field changes from convergent to divergent flow is consistent among all resolutions. Shaded regions correspond to the error on the median estimated from the 16th and 84th percentile in each radial bin.